Evaluating River Ice Elevation, Thickness, and Roughness Using Airborne LiDAR

By

Rouzbeh Hoghooghi Esfahani

A thesis submitted to the Faculty of Graduate and Postdoctoral Studies of the University of Manitoba in partial fulfillment of the requirements for the degree of

Master of Science

Department of Civil Engineering
University of Manitoba
Winnipeg, Manitoba, Canada

Abstract

Monitoring river ice processes is essential for understanding ice-related hydraulic dynamics and potential flood risks. In this study, high-resolution top-of-ice elevation was surveyed using airborne LiDAR, providing fundamental information for characterizing the ice cover. This elevation data alone serves as a critical metric for river ice monitoring. Building on this foundation, two critical river ice parameters, ice thickness and ice surface roughness, were analyzed using a novel integrative approach. To evaluate ice thickness in a fluvial setting, field-measured water level data were combined with remotely sensed data, specifically a high-resolution digital elevation model (DEM) of a fluvial ice cover generated from LiDAR measurements. This approach enabled estimation of ice thickness by leveraging the synergy between in situ observations and advanced remote sensing techniques.

Additionally, the study evaluated the performance and capabilities of the remotely piloted aircraft (RPA) Matrice-350 equipped with the DJI L2 LiDAR payload. The RPA platform demonstrated high precision in capturing both elevation data and surface imagery, making it an effective tool for surveying ice-covered rivers in challenging environments. The results highlight the potential of RPA-mounted LiDAR systems for advancing river ice monitoring and analysis.

Finally, the surface characteristics of river ice were systematically analyzed and classified. By applying statistical metrics, the ice surface roughness was categorized into two distinct groups: smooth and rough. This classification provides valuable insights into the spatial heterogeneity of river ice, with implications for hydraulic modeling and ice-related engineering applications.

This study demonstrates the effectiveness of integrating remote sensing techniques with advanced RPA technology to comprehensively evaluate critical river ice parameters. The resulting dataset

significantly enhances the understanding of the field of river ice engineering and improves the accuracy of numerical modeling by providing essential inputs for ice jam simulations.

Acknowledgments

I have come a long way from home to pursue my master's degree, and throughout this journey, I have been fortunate to receive immense support from many people who have played a vital role in helping me reach this milestone.

First and foremost, I would like to express my deepest gratitude to my partner, my love, whose sacrifices, patience, and unwavering support have paved the way for my success. I am equally indebted to my parents, who, despite the distance, have never spared their love, encouragement, and support throughout these past two years.

I am sincerely thankful to my friends, who have been like brothers to me. Their long-lasting friendship and constant encouragement have been a great source of strength and motivation throughout this journey.

I would like to extend my heartfelt appreciation to my supervisor, Dr. Shawn Clark, whose exceptional guidance, wisdom, and integrity have deeply inspired me. I have learned invaluable lessons from him, both academically and personally. I am also grateful to Mr. Alexander Wall, whose expertise and dedication in the field made the data collection and fieldwork possible. Without his contributions, this research would not have come to fruition.

Finally, I would like to acknowledge the University of Manitoba, Manitoba Hydro, and the Natural Sciences and Engineering Research Council of Canada (NSERC) for their financial and institutional support, which made this research possible.

Table of Contents

List of Figures

List of Tables

Chapter 1 Introduction

1.1 Background and Motivation

As turbulent water becomes supercooled (i.e., water remains in the liquid phase even though its temperature drops below 0 °C) in northern regions of the world, tiny ice particles – called frazil ice - begin to form. As frazil ice particles flow down the river, they can collide and accumulate to form frazil pans. On the other hand, a thin layer of ice may form thermally alongside the riverbanks, known as border ice. The presence of thermally grown border ice and frazil pans moving downstream, combined with factors such as reduced flow velocity, may create conditions for ice accumulation. In some cases, these ice pieces will continue drifting downstream if there are not enough resisting forces to halt their movement. However, they may sometimes interlock and form a phenomenon known as bridging. Once bridging occurs, incoming ice from upstream accumulates behind the stationary cover, causing the ice front to progress upstream —a process known as frontal progression. This can lead to the formation of a thin layer of continuous ice cover.

One particularly concerning river ice process is the formation of an ice jam, which can occur in several different forms (Beltaos, 2008). In late fall or early winter, incoming ice pieces, such as frazil slush, pans, and other ice blocks, may collide with a stationary ice cover, leading to the formation of a freeze-up ice jam. Depending on factors such as the volume and velocity of the incoming ice and the geometry of the river channel, the jam can continue to thicken over time. Alternatively, part of the incoming ice volume may be transported beneath the formed ice cover, a process known as under-cover ice transport.

Another type, known as a break-up ice jam, typically forms in late winter or early spring. As temperatures rise, the strength of the stationary ice cover weakens. At the same time, increased inflows from snowmelt and runoff raise the river's discharge and shear stress. When the applied forces exceed the strength of the ice cover, break-up occurs, mobilizing large ice floes. These floes can accumulate downstream, forming a dense jam that resists the flow. As a result, upstream water levels may rise rapidly, sometimes by several meters within minutes, leading to ice jam flooding, which can be more destructive than typical open-water floods (Hicks, 2016). Water continues to build up behind the jam until the combined action of flow shear stress, the gravitational force of the jam's weight, and hydrodynamic forces at the jam head exceeds the resisting forces, such as the internal strength of the ice accumulation (Beltaos, 2008). This failure can result in the sudden release of water and ice, producing a surge or ice jam wave, commonly referred to as a jave, that moves down the river. Following the release of an ice jam, the downstream reach may experience rapid surges, with water levels rising at rates approaching 0.5 m/min and flow velocities on the order of 10 m/s.

Studying ice jams is crucial for a deeper understanding of this phenomenon and for preventing severe events. Ice jam thickness and roughness are two of the most critical factors in river ice engineering because they both greatly impact river hydraulics. In other words, thicker and rougher ice jams can significantly raise water levels. While these are key features in river ice engineering, other factors like river geometry or the location of ice jams can also affect the hydraulic conditions of rivers.

Monitoring ice processes, such as surveying the top-of-ice elevation profile of an ice jam or collecting water surface elevation (WSE) data during the freeze-up season, can be time-consuming, hazardous, and, in some cases, impractical using traditional field methods. To address these challenges, aerial data collection using Remotely Piloted Aircraft (RPA) has emerged as a reliable and safer alternative for observing and analyzing ice conditions across large spatial extents.

1.2 Literature Review

1.2.1 River Ice Study Methods

Typically, researchers take three different approaches to develop a better understanding of the underlying physics that govern river ice processes. The first approach involves direct measurements by deploying equipment and conducting fieldwork. One of the most significant efforts in this manner has been done by the Water Survey of Canada. Pelletier (1990) reviewed the techniques used by the Water Survey of Canada and other northern countries. This paper discusses data processing techniques and data collection methods, including discharge, velocity, and water depth measurements under ice-affected conditions. Depending on the purpose of the survey, researchers can experience physical injuries due to cold weather and the fragility of ice in rivers, considering the dynamic nature of the formed ice cover.

The second approach uses numerical models. Carson et al. (2011) conducted a vast numerical modeling comparison experiment using different river ice modeling software to simulate the formation of an ice jam. The results illustrated that the models are reliable only when calibrated using actual data from the field; therefore, there is still a need for data collection in the field that involves safety risks for researchers.

The third approach is physical modeling, where researchers design an experimental setup to replicate real-world applications in a laboratory setting. This method provides valuable insights into real-world phenomena, but it also has its limitations. Specifically, accurately simulating real-world conditions – both hydraulic and meteorological – in a laboratory can be particularly challenging in river ice research, leading to potential constraints in the experimental setup.

Up to this point, it is crystal clear that each approach has its own strengths and limitations; therefore, selecting the most suitable method requires careful consideration of multiple factors. This research introduces a novel field data collection approach using remote sensing techniques to significantly reduce safety risks. Moreover, based on the collected data, an analytical framework that integrates direct measurements with post-processing techniques to estimate river ice thickness and roughness with improved accuracy, while minimizing field exposure. Although no numerical modeling was conducted in this research, the outcome of this study can provide a detailed dataset for those developing ice jam models to calibrate and validate their models.

1.2.2 River Ice Thickness

Generally, river ice can thicken through two primary processes. The first is thermal growth, which depends entirely on the heat flux between the ice and the air. Colder air temperatures promote thicker ice; however, due to the insulating effect of the ice itself, the rate of growth beneath the ice slows as it becomes thicker. Border ice is a typical example of thermally grown ice. Cumulative degree-days of freezing (CDDF), which represent the sum of daily average air temperatures below 0°C over a given period, provide a useful index for quantifying this thermal growth. Graf and Tomczyk (2018) demonstrated the effectiveness of CDDF in predicting ice formation on the Noteć River in Poland, where threshold values for ice cover development varied along the channel, ranging from 16°C·d in the upper course to 92.6°C·d in the lower course. Their results further showed that CDDF is a reliable factor not only for predicting the onset of ice cover but also for assessing its persistence throughout the winter season. The second process is mechanical thickening, which occurs when ice pieces collide and consolidate. This type of ice can reach much greater thicknesses than thermally grown ice and often has much rougher characteristics due to the collision and accumulation processes. A massive discharge in a river with an ice cover will cause the shear forces of the flow to overcome the ice strength and cause the ice cover to break and accumulate as a thick ice jam, which causes the water level to rise further. These facts show why researchers have always sought methods to measure, estimate, or calculate river ice thickness.

The thickness of thermally grown ice can be measured by drilling holes, which is a practical and widely used method. However, this approach provides information only at a single location and for one specific point in time. In addition, drilling on river ice involves safety risks that must be carefully considered. In contrast, for mechanically thickened ice accumulations, direct measurement methods are often impractical or nearly impossible due to the irregular and consolidated nature of the ice mass.

In this study, the primary focus is on ice jam thickness; therefore, references to ice thickness pertain specifically to mechanically grown ice. Wazney et al. (2017) conducted research on the Dauphin River to estimate mechanical ice thickness by surveying top-of-ice elevations in relation to previously measured bank elevations. Two approaches were tested for obtaining top-of-ice data: a Real-Time Kinematic (RTK) Global Navigation Satellite System (GNSS) and a terrestrial laser scanner, both of which produced nearly identical results. Eventually, ice thickness was determined by comparing bank elevations surveyed prior to freeze-up with top-of-ice elevations recorded during freeze-up, after the water level had receded and the ice cover had become supported by the bank.

1.2.3 River Ice Roughness

Roughness in general can be characterized in three ways: amplitude roughness, spacing roughness, and hybrid roughness. Each type can be defined using different statistical metrics. In this research, the focus is solely on amplitude roughness, which describes the vertical range of sampled elevations and their variability across a surface, representing the irregularity in its vertical profile (Gadelmawla et al., 2002). Nolin et al. (2018) quantitatively defined surface roughness as the root-mean-squared deviation of surface elevations from a flat reference plane.

In river ice, different levels of amplitude roughness can be observed. Thermally grown ice covers exhibit very low vertical surface elevation variability, indicating a smooth roughness. Juxtaposed ice covers show greater variability in surface elevations compared to thermally grown ice, making them rougher. Ice jams, formed through extreme collisions of ice chunks, display the highest vertical irregularities and represent the roughest type of river ice.

When an ice jam forms, its top surface roughness has been shown to be proportional to its underside surface roughness shortly after formation. This is only temporary, since the flow causes smoothening of the underside of the ice jam over time (Ehrman et al., 2021). Rough ice in the river influences the flow resistance; adding more resistance will decrease the water velocity and lead to a rise in the water level upstream of the ice jam.

When an ice jam forms, its top-surface roughness has been shown to be proportional to its underside surface roughness shortly after formation. This proportionality was demonstrated by Ehrman et al. (2021) through the estimation of top and bottom roughness of newly formed ice jams. Using the Nezhikhovskiy equation (Equation 4) and the estimated ice-thickness values, subsurface Manning's roughness coefficients were derived. The Strickler formula (Strickler, 1923) was then applied to convert measured surface roughness heights into Manning's roughness coefficients. Finally, statistical analyses were conducted to evaluate the relationship between surface and subsurface Manning's roughness values, revealing a proportional correlation between the two.

In river hydraulics, the Manning equation is a widely used empirical formula that relates discharge to cross-sectional area, water depth, friction slope, and a roughness parameter. Equation 1 presents the Manning equation. Under the common assumption of steady, uniform flow, the friction slope is equal to the bed slope, which is then used in the equation. Roughness is represented by Manning's coefficient, an empirical parameter that depends on the characteristics of the channel bed under open-water conditions.

Equation 1
$$Q = \frac{1}{n} A R^{2/3} S^{1/2}$$

In Equation 1, Q represents the discharge, A is the cross-sectional area of the flow, R is the hydraulic radius, which is the ratio of the cross-sectional area of flow to the wetted perimeter, and S is the friction slope. The Manning's roughness coefficient, n, is derived from experimental measurements and reflects the resistance characteristics of the channel. In this equation, all variables must be expressed in SI units; otherwise, when using imperial units, a conversion factor of 1.49 must be applied to the right-hand side of the equation. Manning's coefficient can be determined through back-calculation under controlled conditions. For example, consider a simple rectangular channel with a known bed slope, discharge, water depth, and width. By varying the bed material and substituting the known variables into Equation 1, the value of n can be calculated for each case. As the bed material changes from smooth surfaces such as glass to rougher materials like coarse concrete, the calculated n value increases, reflecting the greater roughness of the surface. Using this approach, reference tables have been developed and are widely used in hydraulics, assigning typical Manning's coefficient values to different channel materials.

The presence of an ice cover alters the Manning's coefficient. Under ice, the velocity distribution divides the flow into two zones: an ice-affected region beneath the cover, and a bed-affected region near the channel bed. The maximum velocity occurs at the interface between these zones. The location of this line is controlled by the relative magnitude of roughness exhibited by each area. If the ice underside is rougher than the bed, this interface shifts downward, enlarging the ice-affected portion of the depth; if the bed is rougher, it shifts upward. On this basis, several equations have been proposed to account for ice roughness by deriving a composite roughness that combines contributions from the ice and the bed. The Sabaneev equation is among the most widely used and is shown in Equation 2 (Uzuner and Kennedy, 1976).

Equation 2

$$n_c = n_b \left[\frac{1+\frac{P_w^i}{P_w^b}\left(\frac{n_i}{n_b}\right)^{\frac{3}{2}}}{1+\frac{P_w^i}{P_w^b}} \right]^{\frac{2}{3}}$$

The variables n_b, n_i, and n_c represent the bed, ice, and composite Manning's roughness, respectively. P_w^i and P_w^b are the wetted perimeter of the ice cover and channel bed, respectively.

Considering ice cover in the rivers, Manning's equation will change in two ways, which is shown in equation 3.

Equation 3 $$Q = \frac{1}{n_c} A {R_i}^{2/3} S^{1/2}$$

In the ice-covered formulation, two terms differ from the open-water Manning's equation: (1) the roughness coefficient (n_c), which is taken as the composite roughness (Eq. 2), and (2) the hydraulic radius, R_i, which uses a modified wetted perimeter. Under open-water conditions, the wetted perimeter P equals the bed perimeter in contact with water. With an ice cover, P also includes the underside of the ice, so it increases. For a given discharge, a larger P reduces R = A/P; therefore, to satisfy Manning's equation, the flow depth must increase to compensate for the reduced hydraulic radius. This shows the importance of the presence of the ice cover in rivers and how it can modify the river's hydraulics.

Ice thickness and ice roughness in the context of river ice were discussed separately in the previous sections; however, some studies suggest there may be a link between ice thickness and Manning's ice roughness coefficient. Nezhikhovskiy (1964) identified such a correlation through direct field measurements of ice thickness and, in his study, proposed an equation relating measured ice thickness to the corresponding Manning's roughness coefficient, as shown in Equation 4.

Equation 4 $$n_i \approx 0.0252 l_n(t_i) + 0.0706$$

In this equation n_i is the under-ice Manning's roughness and t_i is the measured ice thickness. This formulation suggests a potential relationship between ice thickness and its roughness, which will be explored in this study.

1.3 Remote Sensing

Due to the aforementioned safety concerns with field monitoring during the winter, remote sensing is an attractive alternative. Remote sensing technology can be categorized into three different types: 1-Satellite-based remote sensing tools, such as multitemporal tools, including passive microwave synthetic aperture radar (SAR) and LiDAR sensors (Ban, 2016); 2-Aerial-based remote sensing tools can be divided into remotely piloted aircraft (RPA) and manned aircraft. There are multiple RPA sensors, like high-resolution cameras, multispectral, hyperspectral, short/mid-wave range cameras (e.g., thermal), and light-weight LiDAR that can be equipped on RPAs depending on the surveying goals (Yao, et al., 2019); 3- Ground-based remote sensing tools like terrestrial LiDAR, which Wazney et al. (2017) used on the Dauphin River.

Zakharov et al. (2024) conducted a comprehensive review of technologies for river ice monitoring and noted that aerial LiDAR has not yet been applied in this field; the documented LiDAR use pertains to satellite-based systems, primarily for estimating river bathymetry by penetrating the water surface with laser beams. They also highlighted the potential of aerial LiDAR, citing its high precision and accuracy in surface surveying and its capacity to generate valuable datasets for river-ice studies. While they report no aerial LiDAR applications to date, Duguay et al. (2023) conducted an aerial LiDAR survey of the Coaticook River in Quebec. Using 24 GCPs placed on both the ice cover and riverbanks, they achieved an RMSE of 0.06 m. Their work primarily focused on comparing the performance of the photogrammetry-based P1 payload and the LiDAR-based L1 payload, without extending the analysis to ice thickness or surface roughness estimation.

1.3.1 Ice Thickness Estimation Using Remote Sensing Tools

Liu et al. (2023) estimated ice thickness on the Yellow River by utilizing Sentinel-1 SAR image parameters (e.g., VV polarization). The results indicated that the Sentinel-1 SAR's VV polarized coefficient strongly correlates with measured ice thickness, with a 0.702 Pearson correlation coefficient. Another satellite-based research project was conducted by Lindenschmidt et al. (2010) to estimate ice thickness on the Red River in Manitoba using RADARSAT-2 satellite imagery. They reported a good correlation between the HH-backscatter reading and measured ice thickness. HV-backscatter was found to have a better correlation with fresh snow depth. The number of studies using RPA-based methods for ice thickness estimation is limited in river ice fields. However, in lake ice studies, Jin et al. (2024) used ice and ground-penetrating radar (IGPR) equipped on an RPA to estimate ice thickness in two non-freshwater lakes in China. Since the propagation velocities of radar waves are different in different media, they were able to estimate the lake ice thickness using this feature with exemplary accuracy. The RMSE between measured lake ice thickness and estimated lake ice thickness was 0.034 m and 0.010 m on the two lakes that were investigated.

1.3.2 Ice Roughness Estimation Using Remote Sensing Tools

The remote sensing technique of synthetic aperture radar (SAR) is a form of radar that uses the motion of a radar antenna to simulate a larger antenna aperture to produce a finer resolution of two- or three-dimensional structures. Another version of SAR is an interferometric synthetic aperture radar, where two or more SAR images are used to generate digital elevation models (DEMs) that have been used frequently in studies. SAR can be used to estimate ice roughness since rougher surfaces produce more backscatter than smoother surfaces (Dammann et al., 2018). Satellites used for ice roughness estimation have been C-band Sentinel-1, C-band RADARSAT-2, L-band ALOS-2/PALSAR-2, TerraSAR-X, and TanDEM-X. The major problem with utilizing satellite data is that they do not have high spatial resolution (i.e., in the order of 30 m/pixel), which can affect the quality of the results when investigating small-scale structure such as ice roughness. An alternative method uses sensors equipped on RPAs flying at lower altitudes to obtain higher-resolution data. Ehrman et al. (2021) surveyed the Dauphin River using an RPA to collect images from the fluvial ice covers. These images were processed with structure from motion (SFM) photogrammetry to create a DEM. They reported that all DEM-derived roughness metrics produced RPA-measured ice surface Manning's n values that were strongly correlated with ice thickness. Among the statistical metrics tested, the interquartile range (IQR) and standard deviation (SD) were identified as the most effective, demonstrating the strongest correlations with both Manning's roughness and the corresponding ice thickness.

Although several studies were conducted to measure ice thickness and ice roughness on fluvial ice covers, the resolution and accuracy of the results can be significantly improved. LiDAR technology is particularly valuable for capturing topographic data remotely, which is crucial for understanding and modeling river ice dynamics. LiDAR can be deployed on terrestrial, aerial, and satellite platforms, offering flexibility and precision in data collection (Bhardwaj et al., 2016). LiDAR sensors can collect millions of points from a surface, each with accurate spatial coordinates, greatly enhancing the accuracy and reliability of river ice data while minimizing the risks to researchers.

1.4 Ice Jam Numerical Modeling

1.4.1 Introduction to Ice Jam Numerical Models

In river ice engineering, numerical modeling is recognized as one of the most effective approaches for investigating ice jam formation and its associated impacts. Numerical models of river ice are widely applied to evaluate and map ice-jam flood hazards, assess associated risks, and project how the frequency and severity of such events may shift under changing climatic conditions. These models simulate the conditions leading to ice-jam formation by incorporating hydraulic and ice-related factors, and they estimate the resulting backwater levels to help anticipate flooding.

Each modeling framework employs different methodologies to simulate ice jam formation and requires a distinct set of input parameters; however, they are all fundamentally governed by the granular force balance equation, which provides the underlying basis for simulating ice jam processes. In this section, several well-known river-ice numerical models are reviewed, and their capabilities in modeling ice jams are explored based on previous studies. Among many available models developed to simulate river ice processes, particular focus was given to those models capable of simulating ice dynamics related to ice jamming and bridging (Barrette et al., 2024).

1.4.1.1 HEC-RAS

This model allows for the simulation of an ice jam under steady-state conditions. To simulate an ice jam profile using HEC-RAS, several input variables must be specified. Notably, the model does not predict the location of an ice jam; instead, the user must manually define the toe and head of the jam. As with any numerical model, boundary conditions such as known water surface elevation or normal depth for the downstream boundary conditions and discharge for the upstream boundary conditions are required. Additional key inputs include the thickness of the sheet ice cover, as well as Manning's roughness coefficients for the riverbed and for the underside of the ice cover or jam. In HEC-RAS, the user can either assign a fixed roughness value at each cross section or specify a roughness coefficient that varies with the computed ice thickness. While this research focuses on top-of-ice elevation, ice thickness, and ice roughness, HEC-RAS requires other inputs, such as the maximum allowable flow velocity beneath the jam (Beltaos, 2001) or the internal friction angle of the jam (Beltaos & Burrell, 2010). Further details on these parameters can be found in the cited literature.

When performing ice jam simulations in HEC-RAS, the model determines ice thickness and the corresponding water levels through an iterative procedure that continues until an equilibrium jam profile is achieved. The hydraulic calculations are performed in the downstream-to-upstream direction, while the ice thickness is computed in the opposite direction, from upstream to downstream, reflecting the physical process of ice accumulation. This iterative approach ensures that the force balance between driving and resisting forces is satisfied along the jam.

After developing a model, the first step is calibration, which critically depends on the availability of field data. Lindenschmidt et al. (2025) reported that blind tests on numerical models in previous studies demonstrated considerable variability in their performance, highlighting the importance of field data for reliable calibration. In this context, Beltaos and Tang (2013) emphasized that observed water levels and top-of-ice elevations, when available, can serve as valuable references for graphical comparisons in calibration runs.

1.4.1.2 River 1D

This model, developed at the University of Alberta, is capable of simulating ice jam formation under unsteady flow conditions. Blackburn and She (2023) applied it to both idealized and real-world channel networks. Their results showed strong agreement with observed data, particularly when jam consolidation was considered, highlighting River1D's effectiveness in capturing ice jam dynamics under variable flow scenarios. In their study, the authors validated model accuracy using recorded top-of-ice elevations and water surface elevations (WSE). Several surveyed top-of-ice points were excluded from the dataset because they were identified as stranded ice blocks, remnants left behind after the jam moved downstream, that produced unrealistically high elevation values. This limitation arose from the use of traditional manual surveying methods, which restricted measurements to top-of-ice points located near the riverbank. In terms of roughness coefficient, a constant Manning's roughness coefficient of 0.055 was applied beneath the ice jam throughout the simulations.

1.4.1.3 RIVICE

RIVICE is a one-dimensional hydrodynamic model that simulates ice cover formation and ice jam development in rivers. It solves the fundamental equations of unsteady open-channel flow, which describe the conservation of water volume and momentum, and incorporates routines for ice processes such as juxtaposition, shoving, and submergence (Lindenschmidt, 2017). Model performance depends on parameters describing hydraulic resistance and jam strength, including ice underside roughness, porosity, and internal stress ratios. Calibration is typically based on observed water surface elevations, and when available, ice thickness measurements, making RIVICE a practical tool for assessing ice jam hydraulics and flood risk. Lindenschmidt et al. (2012) developed a numerical model of the Dauphin River in Manitoba, covering a 52 km reach, and calibrated the open-water conditions using nine surveyed water surface points, including one located in a steep section where the profile dropped abruptly. For ice-covered conditions, five top-of-ice elevation points were used, three of which were also situated within the steep reach. Given the river's length, this limited number of calibration points may have been insufficient to achieve a fully reliable model calibration.

1.4.1.4 RIVJAM

The RIVJAM model is a one-dimensional, steady-state numerical model for river ice jams. Key physical processes represented in RIVJAM include ice jam formation and thickness distribution, internal jam strength, and the hydraulic backwater response upstream of the jam. Beltaos and Burrell (2010) applied the RIVJAM numerical model to simulate ice jam formation on the Matapédia River, Québec, using detailed field data from the 1994 and 1995 breakup events. At these sites, an Ice-Jam Profiler (IJP) was deployed to capture ice thickness profiles, and both ice thickness measurements and surveyed water surface elevations were used to validate the model's performance.

1.4.1.5 CRISSP 2D

CRISSP2D is a two-dimensional depth-averaged numerical model that simulates river ice processes by coupling hydrodynamic and thermal components. It was developed as part of the Comprehensive River Ice Simulation System (CRISSP) by generalizing the earlier DynaRICE model (Shen et al., 2000) and extending it to include thermally related processes (Liu et al., 2006). CRISSP2D requires input data on meteorological conditions (e.g., air temperature, wind, cloud cover, precipitation), hydraulic and geometric characteristics (e.g., bathymetry, boundary conditions, control structures), and thermal/ice conditions (e.g., inflow water temperature, initial ice cover, ice discharge). Building on this framework, Wazney et al. (2019) developed a CRISSP2D model on an idealized channel representing the lower Dauphin River. By incorporating thermal strengthening into the simulations, they demonstrated that the rate of surface ice crust development can significantly influence the mode of ice jam formation. At low strengthening rates, mechanical thickening is more likely to occur. In contrast, at higher rates, the crust provides sufficient resistance to incoming ice, leading to frontal progression and the formation of a thinner, continuous ice cover produced mainly through thermal rather than mechanical processes. They reported that field measurements like WSE and ice thickness during freeze-up will allow the model calibration and validation.

1.4.2 Integration of Research Findings into Ice Jam Numerical Modeling

As discussed in the previous section, numerical models require reliable datasets for development, calibration, and validation. The importance of comprehensive river ice datasets for these purposes has been demonstrated through several examples from the literature. Also, Lindenschmidt et al. (2025) conducted a model comparison study on a 73.5 km reach of the Athabasca River at Fort McMurray, where six river-ice models (CRISSP2D, ICESIM, HEC-RAS, River1D, RIVICE, and VARY-ICE) were tested under identical boundary conditions. The objective was to evaluate each model's ability to reproduce ice-jam profiles and water levels, while assessing their respective data requirements and computational approaches. For calibration, 13 observed high-water mark points were used to adjust roughness coefficients and ice-jam strength parameters, ensuring a consistent basis for comparison across models.

Building on that discussion, it is important to highlight a common challenge in the calibration process of ice jam models. Typically, model calibration involves adjusting key parameters to produce results that match validation data. However, this process, mainly when carried out without sufficient experience, can introduce errors. For example, ice jam models often rely heavily on inputs such as initial ice thickness and Manning's roughness. During the calibration process, the required parameters can be adjusted to produce a good match with measured data (i.e., WSE, for instance) for validation purposes, while at the same time computing an unrealistic ice thickness compared to actual physical conditions.

In contrast, when reliable estimates of ice thickness or roughness are available from field measurements, they can be incorporated into the model to improve the calibration process. For example, a more accurate initial guess of ice thickness can be prescribed, which enhances the efficiency of simulating jam thickness given the HEC-RAS limitation of 101 iterations per run. Similarly, a well-constrained estimate of the roughness coefficient can be fixed in the model, thereby reducing the number of free parameters that require calibration. This helps to constrain the solution space and lowers the risk of arriving at a result that appears accurate but is based on incorrect assumptions. In other words, by minimizing the number of uncertain parameters, the model calibration becomes more physically meaningful and robust.

To address this need, while also acknowledging the hazardous and labor-intensive nature of data collection near rivers during freeze-up and break-up periods, one of the most comprehensive river ice datasets to date was successfully captured during the winters of 2023/24 and 2024/25. This dataset includes continuous top-of-ice elevation profiles, continuous water surface elevation (WSE), ice thickness profiles, and detailed insights into the surface roughness of the ice cover and ice jams along the Dauphin River. Overall, this comprehensive dataset represents a valuable resource for future ice jam model development. The methodologies used in this study can be replicated in other regions to enhance understanding of the complex processes involved in ice jam formation.

1.5 Objectives

Previous studies on river ice have focused on understanding fluvial ice cover dynamics and ice jam formation by measuring or estimating parameters such as ice thickness, often relying on traditional field-based methods that are spatially limited and potentially hazardous. This research presents a novel approach using RPAS-mounted airborne LiDAR to acquire high-resolution, continuous top-of-ice elevation data over extended river sections, enhancing our understanding of fluvial ice processes, particularly those associated with freeze-up ice jams.

The main objectives of this work are as follows:

- Evaluate the capability of RPAS-mounted LiDAR to accurately acquire high-resolution top-of-ice elevation data over an extended section of fluvial ice cover along the Dauphin River.
- Develop a processing workflow to convert a high-resolution DEM of an ice-covered river into a 1D streamwise ice elevation profile.
- Assess the feasibility of estimating continuous ice thickness profiles by combining high-resolution top-of-ice elevation data from LiDAR with water surface elevation data.
- Quantify river ice surface roughness using RPAS-mounted LiDAR data and evaluate its relationship with ice jam thickness.
- Compare roughness estimates derived from LiDAR data with those obtained using Structure-from-Motion (SfM) photogrammetry.
- Provide a detailed dataset of river ice parameters collected over two freeze-up periods along the Dauphin River for use in calibrating and validating numerical ice jam models.

1.6 Study Area

The Dauphin River is located approximately 250 km north of Winnipeg in Manitoba, Canada. This 52 km-long river connects Lake St. Martin to Lake Winnipeg, as shown in Figure 1. It features a gentle bed slope of 0.029% over the upstream 40 km, followed by a steeper 12 km downstream section with a slope of 0.16% (Clark & Wall, 2016). The steeper gradient in this reach results in higher flow velocities and increased turbulence, which promote the formation of frazil ice. The average river width in this section ranges from 80 to 110 meters.

Clark and Wall (2016) conducted an extensive field setup on the Dauphin River, establishing multiple monitoring sites along both the upstream and downstream sections. Due to the remote nature of the area and lack of cellular service, surveying posed significant logistical challenges. To address this, a rebar post was installed and surveyed at each site to serve as a control point for future surveys. Each site was labeled with the prefix "DR" (for Dauphin River) followed by a number increasing from upstream to downstream.

This study focuses on sites DR04 to DR07, which are located within the steeper downstream 12 km stretch of the river before it enters Lake Winnipeg. This section is particularly relevant due to its dynamic ice conditions and the occurrence of ice consolidation events and associated surge waves that have historically contributed to significant ice thickening. Wazney et al. (2019) reported that such surge wave events led to discharges exceeding 400 m^3/s—more than double the steady discharge—resulting in mechanical thickening of the ice cover near site DR06, with maximum ice thicknesses ranging from approximately 4.0 to 5.3 meters. According to the Water Survey of Canada, the open-channel discharge of the Dauphin River immediately prior to freeze-up was approximately 65 m^3/s in the 2023/24 season and 75 m^3/s in the 2024/25 season.

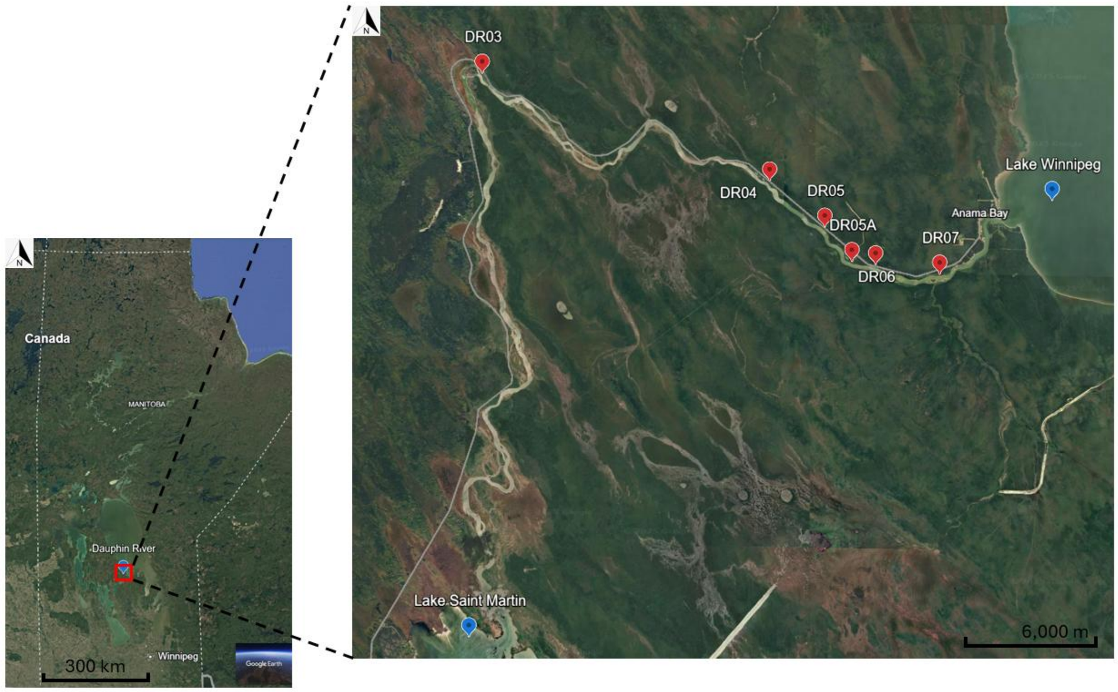

Figure 1. Study area map of the Dauphin River, Manitoba, Canada, illustrating the locations of all survey sites used for ice monitoring and data collection.

Chapter 2 Field Monitoring Program

Two field monitoring campaigns (2023/24 and 2024/25) were undertaken to characterize hydraulic conditions. Water-level and temperature loggers and trail cameras were installed prior to freeze-up and retrieved after breakup, capturing stage variations through freeze-up and breakup and their relation to air temperature. This section details deployment/retrieval methods and analyzes the stage records. Within this dataset, jam formation is consistent with consolidation (mechanical) jamming: frazil slush and pans are mobilized by flow shear to raft and stack until a critical thickness is reached that resists the prevailing hydraulic stresses (Beltaos, 2008). Trail-camera imagery together with the water-level record documents the onset, growth, and stabilization of the jam, which is characteristically thick and rough and can induce rapid stage rises that pose risks to nearby communities, even on rivers without prior open-water flooding.

2.1 Dauphin River Field Work Background

Extensive fieldwork has been conducted on the Dauphin River over several years to investigate river ice processes, particularly in the steeper downstream section where dynamic ice behavior frequently occurs. Clark and Wall (2016) established a network of monitoring sites along the river, implementing fixed survey benchmarks and deploying level loggers to measure water levels continuously over the freeze-up and break-up seasons. These sites served as a foundation for subsequent studies. Wazney et al. (2019) expanded on this by documenting the hydraulic and ice dynamic responses to freeze-up consolidation events, including rapid surge waves that caused mechanical thickening of the ice cover. Their observations included detailed field measurements of water surface elevations, ice thickness (at a handful of locations), and water temperature profiles during and after ice jam events. Building on this foundation, Ehrman et al. (2021) introduced remotely piloted aircraft (RPA) photogrammetry as a novel approach to estimate ice surface roughness across multiple sites on the lower Dauphin River. This method provided high-resolution digital elevation models (DEMs) of the ice cover surface and enabled quantitative analysis of roughness height using statistical metrics such as standard deviation and interquartile range. Collectively, these field campaigns have established the Dauphin River as a critical natural laboratory for advancing the understanding of river ice mechanics and hydraulics under real-world freeze-up conditions.

2.2 Equipment for In-Situ Data Collection

2.2.1 Water Level Logger, Barro Logger, Temperature Logger, and Trail Cameras

For this research program, the focus was on the steeper, lower Dauphin River. At each site one Solinst Levelogger 3001 (accuracy ±0.01 m, frequency 8 minutes) was mounted and secured in the middle of a steel angle iron bar using steel rebar tie wire. A suitable location close to the riverbank with adequate depth and preferably low water velocity was selected to prevent losing the equipment due to the high water velocity. The angle iron bar was then hammered into the riverbed with two pieces of rebar to ensure it would remain stationary throughout the whole winter season. After the deployment of each level logger, the water surface elevation at the logger location was surveyed using an RTK GNSS system. These elevation measurements are essential for converting the pressure data recorded by the loggers into accurate water surface elevations. Section

2.2.2 outlines the procedure for capturing water surface elevation data using an RTK GNSS base and rover setup.

One barometer logger was placed at the meteorological station near site DR03 to be used in correcting water levels, compensating for atmospheric pressure. Using the same installation method, two Seabird SBE 56 water temperature sensors (accuracy ±0.002°C, sampling frequency 1 minute) were installed at sites DR03 and DR03d.

In this study, Moultrie M-1100i digital game cameras were used to monitor ice surface conditions and capture temporal changes in the ice cover. This high-resolution trail camera is specifically designed for remote environmental monitoring and is particularly effective in field settings where direct observation is limited due to access constraints. The M-1100i is equipped with a 12.0 MP image sensor and supports still image capture at pre-defined intervals, making it suitable for long-term observation. A total of seven trail cameras were deployed at the study sites, each mounted on a tree and positioned to provide a clear view of the river channel. The cameras were securely fastened using mounting straps. They remained in place throughout the winter season to ensure continuous image collection and facilitate visual observation of ice jam formation and break-up events. In section 2.3, images for each site will be provided to confirm the estimated start of the freeze-up period. A summary of the equipment installed in the river, along with its recovery status for both years, is outlined in Table 1.

Table 1. A summary of deployed and retrieved equipment in two consecutive field campaigns

Winter 2023/24			Winter 2024/25		
Site	Equipment	Retrieval status	Site	Equipment	Retrieval status
DR07	Level logger	☑	DR07	Level logger	☑
DR07	Trail camera	☒	DR07	Trail camera	☒
DR06	Level logger	☑	DR06	Level logger	☑
DR06	Trail camera	☑	DR06	Trail camera	☑

DR05a	Trail camera	☒	DR05a	Trail camera	☑
DR05	Level logger	☑	DR05	Level logger	☑
DR05	Trail camera	☒	DR05	Trail camera	☑
DR04	Level logger	☑	DR04	Level logger	☑
DR04	Trail camera	☑	DR04	Trail camera	☑
DR03	Level logger	☑	DR03	Level logger	☑
DR03	Trail camera	☑	DR03	Trail camera	☑
DR03	Barro logger	☑	DR03	Barro logger	☑

2.2.2 Real-time kinematic (RTK) Global Navigation Satellite System (GNSS) Base and Rover

The SP60 GNSS receiver, manufactured by Spectra Precision, is a high-accuracy, real-time kinematic (RTK) system used in this research for land surveying and geospatial data collection. It operates with a base and rover configuration. The base unit is set up at a fixed location (i.e., control points in this case), tracking GNSS satellites to provide a reference point. The base transmits correction data to the rover using radio connections to ensure high precision for data collection. The rover is a mobile unit that collects geospatial data across the survey area. It communicates with the base and uses correction data to achieve a centimeter-level accuracy. The manufacturer reported horizontal accuracy of ±8 mm + 1 ppm and vertical accuracy of ±15 mm + 1 ppm; however, multiple factors can influence the accuracy of this system, including the distance between the base station and the rover or the quality of the GNSS signal (Spectra Precision, 2016).

For this research, an RTK-GNSS base and rover equipment were utilized for multiple purposes; however, in this section, the procedure for capturing the WSE will be provided. At each field site, the base station was set up on a control point and connected to the controller, where the whole mission and data collection were controlled. After gaining a proper connection with the available satellites, the rover was started and connected to the base station. No actual assessment was conducted; however, based on field experience, the range for a proper connection between the base station and the rover was determined to be less than 1.5 km. Using the RTK-GNSS rover, the WSE at each site was measured and recorded immediately after each logger was deployed. This reference WSE, matched to the logger's simultaneous pressure reading, was used to convert subsequent pressure measurements into WSE values until the logger was moved or retrieved. The resulting WSE data are presented and discussed in the following section.

2.3 Water Level, Trail Camera, and Temperature Analysis

2.3.1 Winter 2023/24

According to data obtained from the temperature logger deployed near site DR03, the water temperature dropped to - 0.1°C on November 21, 2023. This condition, known as supercooling, marks the onset of frazil ice formation in the river. Another key factor required for frazil ice generation is turbulence. Given the relatively steep slope of the Dauphin River at the study site, the flow velocity is high enough to generate sufficient turbulence to support frazil ice development. Using a pre-developed HEC-RAS model of the Dauphin River at the Hydraulic Research and Testing Facility (HRTF), the open-water conditions at the study sites were simulated to illustrate the hydraulic properties of flow near these locations. The results were summarized in Table 2.

Table 2. Hydraulic properties of the Dauphin River under simulated open-water conditions using the HEC-RAS model (November 2023, prior to freeze-up; discharge = 65 cms)

	Study sites			
Hydraulic properties	DR07	DR06	DR05	DR04
WSE (m)	219.17	222.06	226.9	231.91
Thalweg (m)	218.49	221.09	226.17	230.95
Maximum Depth (m)	0.68	0.97	0.73	0.96
Velocity (m/s)	0.97	1.43	1.49	1.51
Reynolds number	5.89×10^5	1.24×10^6	9.71×10^5	1.29×10^6
Froude number	0.52	0.72	0.79	0.65

As shown in Table 2, the flow velocity, ranging from 1.0 to 1.5 m/s, resulted in Reynolds numbers between 5.89×10^5 at site DR07 and 1.24×10^6 at site DR06. Since values below 2000 indicate laminar flow and values above 4000 mark the onset of turbulence, the observed Reynolds numbers are approximately 150 to 300 times higher than the threshold for turbulent flow. Such high velocities and Reynolds numbers promoted the turbulence necessary for the initiation of frazil ice formation. The reported Froude numbers for each site indicate that, although the flow in this stream remains subcritical (i.e., $Fr < 1$), the values are considerably higher than those typically observed in natural rivers (i.e., 0.05–0.3). This provides further evidence of the highly energetic flow in the Lower Dauphin River, driven by its relatively steep slope.

Figure 2 shows the water temperature in the Dauphin River between November 21 and November 24. As illustrated, supercooling occurred over a short period during the night of November 21. Following this, the release of latent heat due to the formation of frazil ice caused the water temperature to rise slightly, stabilizing between approximately -0.04°C and -0.02°C. These observations and historical records of the same sites for previous years suggest that freeze-up ice jam formation was likely to occur downstream of the Dauphin River in the days that followed.

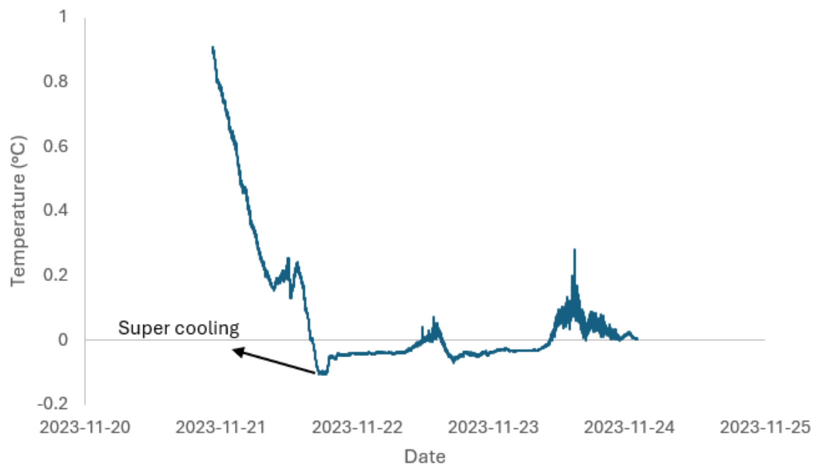

Figure 2. The water temperature during the supercooling event was recorded at site DR03.

The water surface elevation recorded from mid-October 2023 to mid-July 2024 is plotted and shown in Figure 3, where the black oval indicates the freeze-up period, while the red oval shows the break-up event. Based on the figure, a noticeable rise in water level was observed at site DR07 on November 22. Shortly afterwards, water levels began to rise at the downstream sites, progressing sequentially toward DR03. This delay in the stage response demonstrates the frontal progression of the ice cover from downstream to upstream. As the freeze-up ice jam formed and advanced upstream, it influenced water levels at each site, resulting in a staged increase along the river.

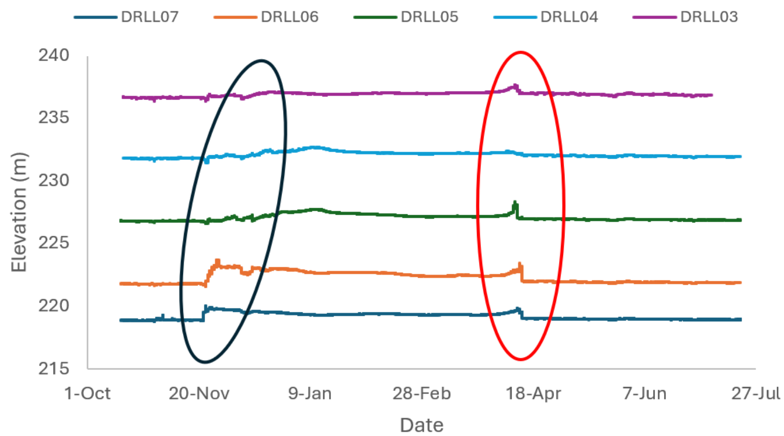

Figure 3. Water surface elevations of study sites during the year 2023/24.

Figure 4 presents a sequence of images captured by the trail camera at site DR06, illustrating the progression from frazil ice formation to the development of a stationary ice jam. Figure 4a shows the initial generation of a large volume of frazil ice, which can be seen floating on the water surface as it travels downstream (from right to left). The date of this image aligns with the supercooling event recorded by the temperature logger, confirming the onset of supercooling conditions. Figure 4b displays the scene on the following day, where the frazil ice, or ice flocs, have started to accumulate. The formed ice was stationary for a period (i.e., 5 hours), and then it started moving downstream, accompanied by a drop in water level of 20 cm.

Figure 4c documents a subsequent ice-accumulation episode along the bank adjacent to the trail camera. The image sequence and water-level record indicate a more forceful accumulation than earlier events, characterized by a 40 cm rise in stage followed by a 27 cm drop. Between Figure 4c and Figure 4d (a one-day gap on 26 November), continued transport of ice from upstream occurred. In addition to the stationary cover near the camera-side bank, a very thin stationary sheet developed along the opposite bank, further increasing the water level. At 20:50 on 28 November, a major collision event occurred in which large ice floes impacted the pre-existing accumulation. Because the event took place in darkness, no coincident imagery is available. In the 29 November image (Figure 4e), large ice pieces are clustered along the bank closest to the camera, suggesting that the incoming ice forced the fixed cover shoreward. The final image (Figure 4f) depicts a stable ice jam at site DR06; thereafter, the water-surface-elevation (WSE) record exhibits no further abrupt stage fluctuations prior to breakup. An open mid-channel lead visible in Figure 4f conveyed flow past the jam, facilitating the final reduction in stage and subsequent stabilization of conditions.

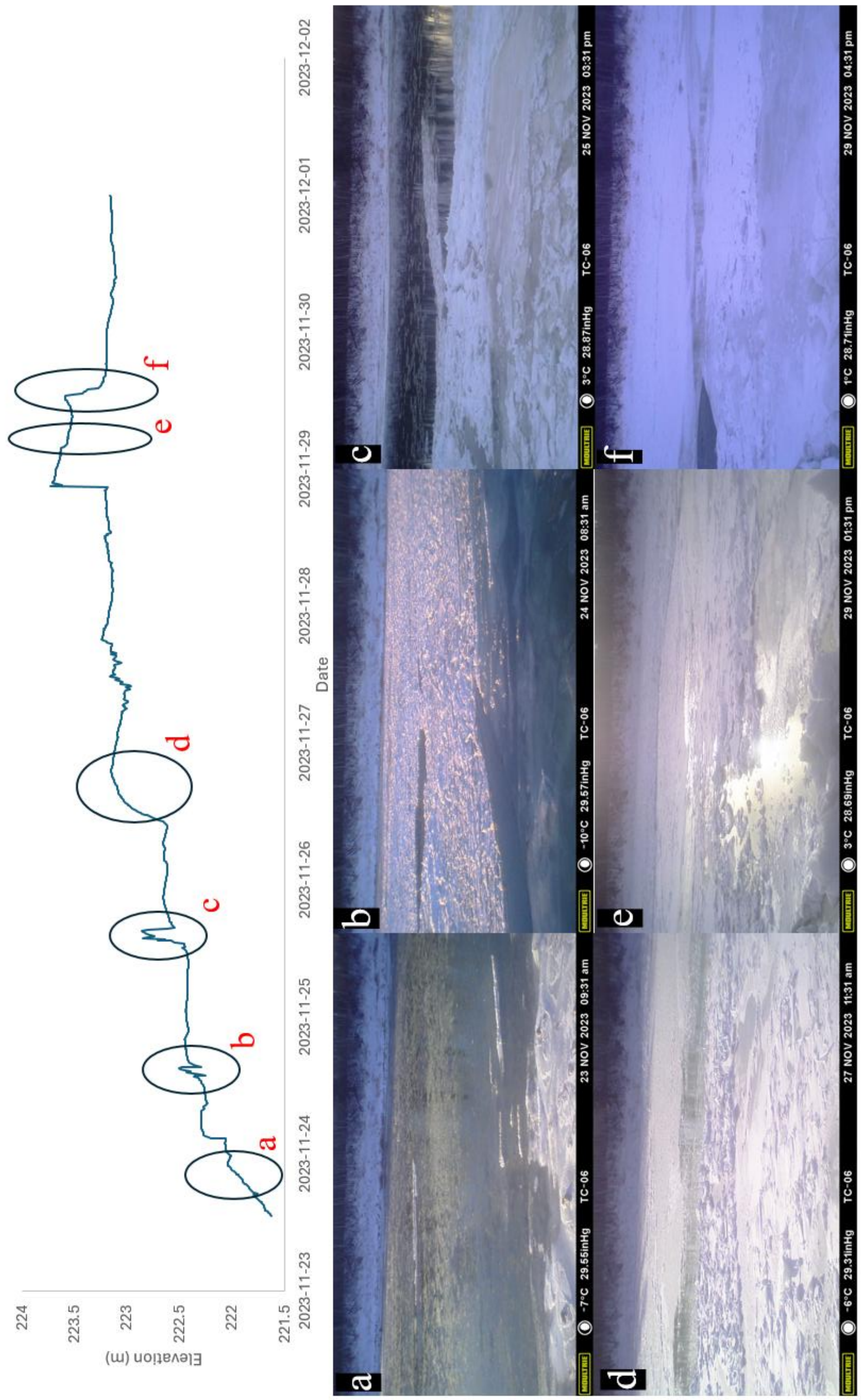

Figure 4. A sequence of images from the trail camera at site DR06 for the winter of 2023/24 shows the generation of frazil ice to the formation of a stationary ice cover.

During the spring of 2024, rising temperatures led to increased snowmelt, resulting in a higher inflow into the Dauphin River. At the same time, warmer air temperatures weakened the existing ice cover. As discharge increased, inflow exceeded the river's conveyance with the jam in place, causing the upstream water level to rise. The water level continued to increase until the shear stresses from the stored flow and other forces acting to destabilize the jam overcame the resisting forces of the stationary jam, causing its release. Once the jam was released and mobilized downstream, it resulted in a rapid drop in water level and the transport of ice pieces farther downstream. Figure 5 shows the water level rise caused by increased spring discharge while the ice jam remained stationary, followed by a sudden drop upon the release of the jam at sites DR06 and DR07.

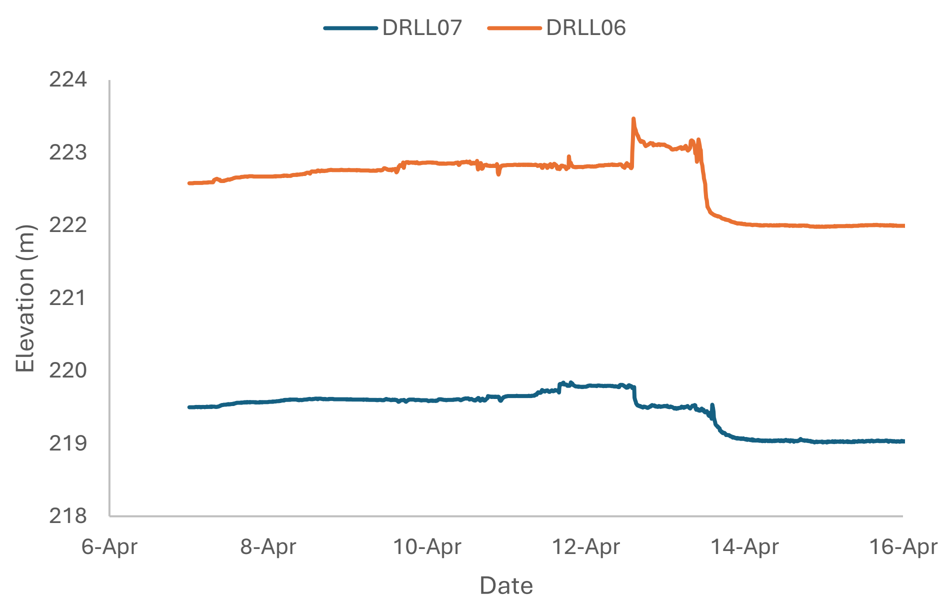

Figure 5. Water surface elevations at sites DR06 and DR07 during the break-up period of the 2023–24 winter.

2.3.2 Winter 2024/25

The same set of instrumentation was deployed and retrieved during the winter of 2024/25. The recorded water surface elevations for the study sites, ranging from DR03 to DR07, are shown in Figure 6. According to discharge data from the Water Survey of Canada, the open water discharge in fall 2024/25 was approximately 10 m^3/s higher than in fall 2023/24. Combined with a change of air temperature pattern compared to the previous year, this led to higher water levels during the freeze-up period in 2024/25. Furthermore, the water level rise at sites DR05 and DR04 was more pronounced and abrupt than in 2023/24, suggesting the formation of a thicker and rougher ice jam during that winter. Following the freeze-up period, an unexpected and dramatic drop in water level was observed in the data recorded by the level logger at site DR06. This drop was abnormal and inconsistent with the patterns recorded at the other sites, which continued to follow the expected trend. This issue is believed to have occurred because the thick ice jam that formed at DR06 may have become grounded, causing the water around the logger to freeze. As a result, the sensor was likely isolated from the actual water surface, preventing it from capturing accurate and reliable data. Although the logger appeared to resume normal function after March, its data remains questionable, as it failed to capture the sudden rise in water level associated with the breakup period, an important indicator observed at the other sites.

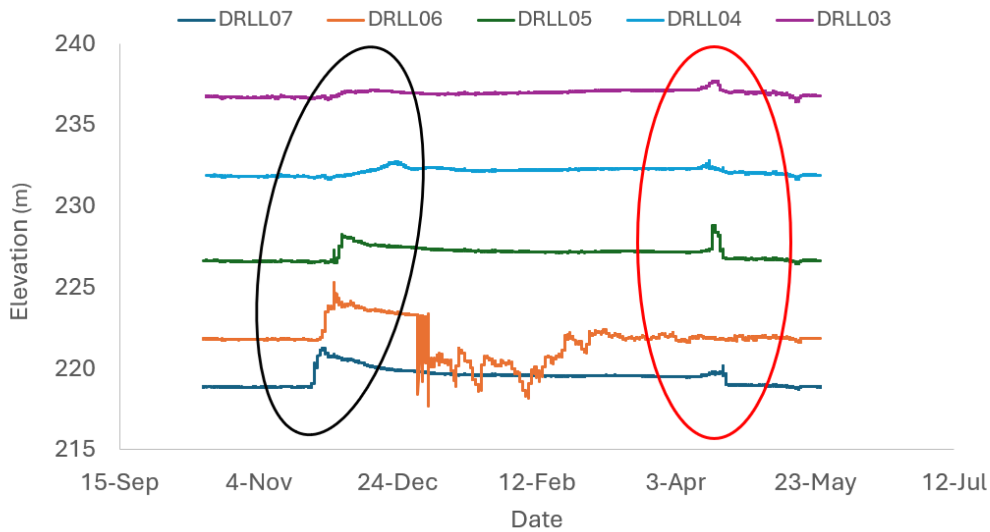

Figure 6. Water surface elevations of study sites during the year 2024/25.

During the freeze-up processes of winter 2024/25, several major events were recorded using level loggers, indicating a rapid rise in water levels within a very short period. Figure 7 shows the water surface elevation plot alongside two pictures of the exact location at site DR06, demonstrating ice jam formation. In this event, the water level increased by 1.5 meters in just sixteen minutes. Figure 7a depicts the situation just before the jamming, while Figure 7b shows the next hour when the jam formed at site DR06. Similar events occurred in 2018/19 at the same study site, which has been extensively studied by Wazney et al. (2018).

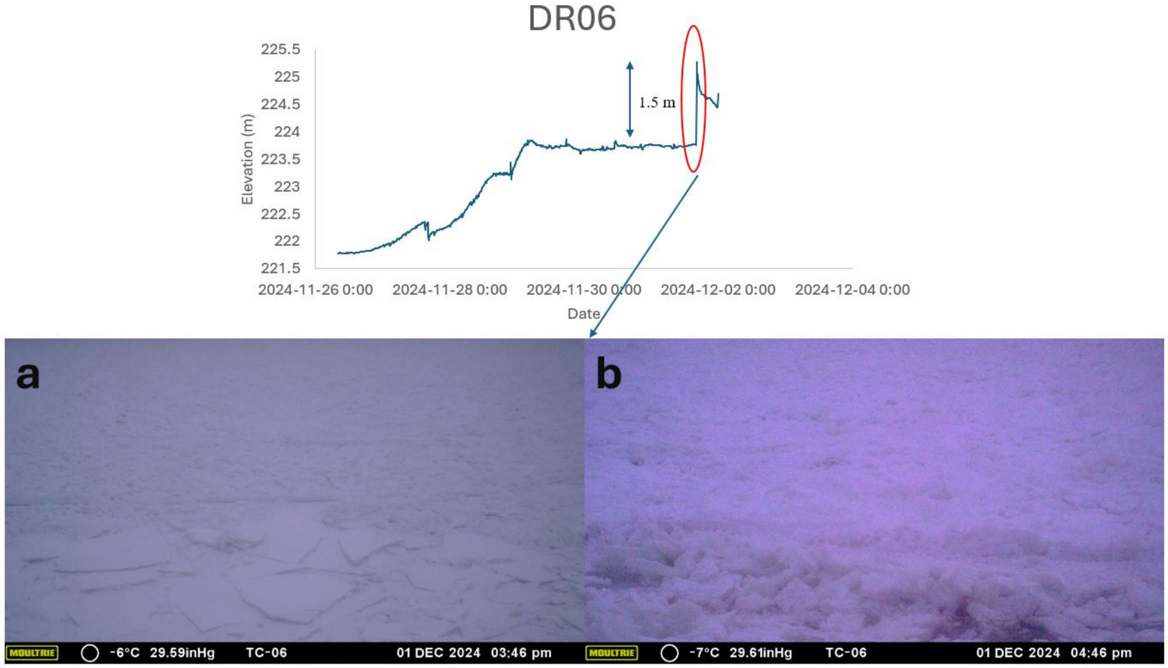

Figure 7. Top: WSE record (26 Nov–2 Dec 2024) showing a 1.5 m stage rise; the circled spike indicates a rapid fluctuation during consolidation.
Bottom: Trail-camera images (1 Dec 2024): (a) stationary accumulation following a gradual stage increase (27–30 Nov); (b) rough, hummocked surface after a major consolidation on 1 Dec.

Similar to the previous year, the breakup in winter 2024/25 occurred in mid-April. A steady rise in water levels began around April 16 as increasing discharge progressively intensified the hydrodynamic forces acting on the stationary jam. Once these forces exceeded the resisting strength of the accumulation, the ice began to mobilize in bursts, breaking apart and drifting downstream until the section was cleared. The breakup process lasted approximately one week, with conditions stabilizing by April 23–24.

In this Chapter, key aspects of freeze-up ice jam formation have been discussed to highlight the importance of parameters such as ice thickness and roughness, and how they can significantly influence potential flooding events. The recorded water surface elevations at sites DR04 to DR07 will be used as validation data in section 4.2, where the extracted water surface elevations from the DEM will be compared to the values measured in the field.

2.4 Top-of-Ice Profile

During the winter season of 2023/24, a field trip was conducted in February to observe the ice jam that had formed that year. A total of 18 top-of-ice elevation points were surveyed using an RTK-GNSS base and rover system, following the same method outlined in Section 2.2.2. These points were collected near the riverbanks and may not fully represent the actual top-of-ice elevation across the channel. However, given the limitations of traditional survey methods, which typically only allow data collection near the banks, these points will still serve as a basis for comparison. In the next chapter, these field-surveyed elevations will be compared with those obtained using the remote sensing approach. Figure 8 shows the manually surveyed points collected with the RTK-GNSS system.

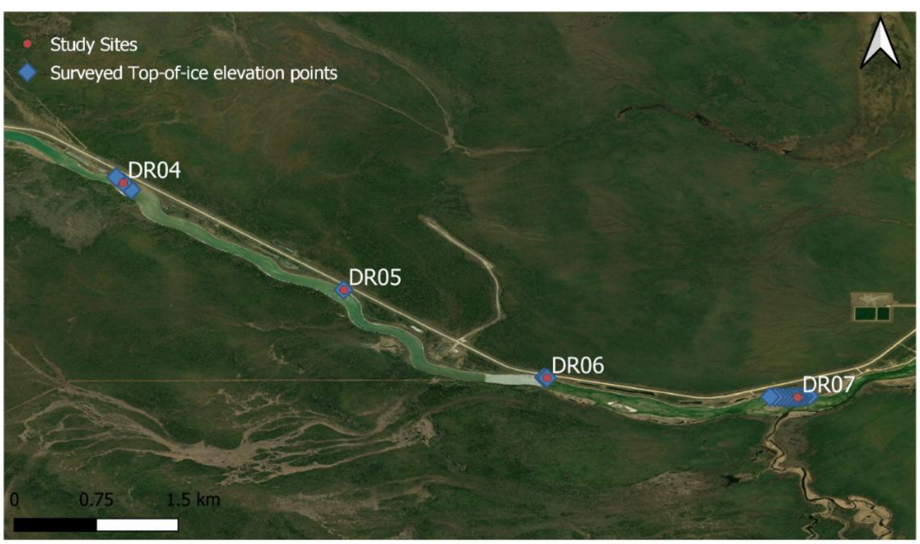

Figure 8. Location of surveyed top-of-ice elevation points along the study sites.

Chapter 3 DEM Generation and Top-of-Ice Elevation Extraction

3.1 Field Data Collection

This study introduces LiDAR as an innovative and highly precise method for acquiring continuous profiles of fluvial ice covers, offering a significant advancement over traditional point-based or cross-sectional surveying techniques. Unlike manual ice-thickness measurements or conventional ground-based surveys, LiDAR provides dense, spatially continuous elevation data that can capture subtle variations in surface morphology across large river sections within a short time. For this research, field acquisition was carried out using a DJI Matrice 350 RPA equipped with a Zenmuse L2 LiDAR sensor, which together enabled high-resolution mapping of the Dauphin River under challenging winter conditions. In this study, to ensure accurate georeferencing of the spatial data, ground control points (GCPs), constructed from plywood and painted as high-contrast red–black targets (0.5 × 0.5 m), were deployed across the survey area and used during data processing.

3.1.1 Winter 2023/24

In February 2024 (winter 2023/24), data collection began at site DR07 and proceeded upstream toward site DR04. All missions were preplanned in the office, and the initial flight at DR07 was flown at an altitude of 100 m with a nominal airspeed of 15 m/s. The total flight time was approximately 21 minutes; however, due to cold air temperatures, the batteries discharged more quickly than expected, preventing the survey from being completed in a single flight. As a result, the RPA returned to the base station, and after replacing the batteries, the flight resumed and the survey was successfully completed. For subsequent missions, the flight altitude was reduced to 75 m to minimize potential interference from fog and moisture that could affect the quality of the LiDAR dataset. Three GCPs were considered for every site to help determine whether GCPs were required at all and to assess their impact on measurement accuracy. Based on the triangulation method suggested by Zhang et al. (2022), three GCPs were placed at each site to form a triangular configuration. This approach was particularly suitable given that it was our first experience surveying with airborne LiDAR using RTK GNSS positioning. By following this method, an evaluation was conducted to determine whether three well-distributed GCPs would provide sufficient georeferencing accuracy for the project and to inform adjustments for future missions. GCPs were surveyed using the Trimble/Spectra Precision SP60 RTK GNSS base-and-rover system. GCPs were positioned with an approximate spacing of 35 m between each one and at different elevations. The GCP locations for site DR04 are shown in Figure 9. One of the main concerns for planning the mission was the range of the RPA RTK positioning system. Based on our experience, the range of a stable connection between the RPA and the RTK positioning system base station is approximately 1.5 km, depending on the site's topography. The length of the Dauphin River between sites DR04 and DR07 is approximately 9 km. Due to the limitations of the RPA's RTK system range, the surveying mission was divided into five separate missions. It should be noted that two separate missions were performed at site DR05 to overcome the limitation of the RPA's RTK range. At each site (DR04 to DR07), pre-existing control points (i.e., semi-permanent rebar driven to refusal) with known positions were utilized. These control points were employed to establish both the RPA's RTK positioning system base station and the RTK-GNSS surveying base station.

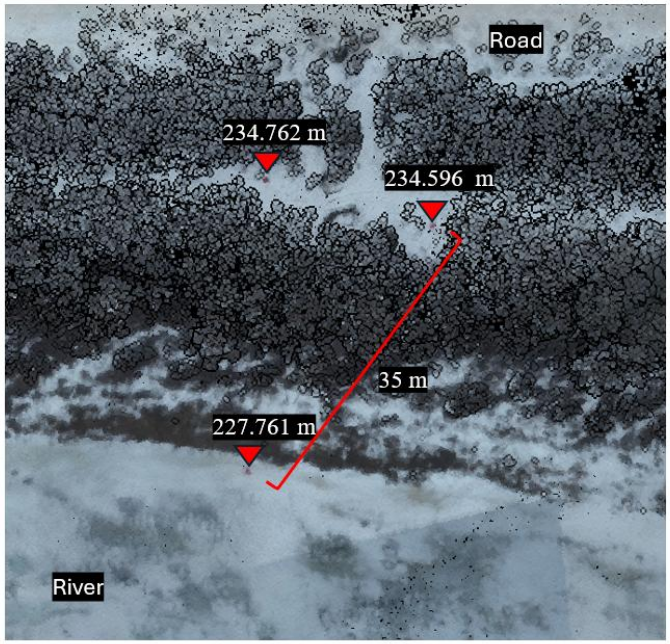

Figure 9. Configuration of GCPs at site DR05 in winter 2023/24.

3.2 Data Processing

The raw LiDAR data, which includes files such as point coordinates, calibration files, and recorded images captured during the flight, was processed using DJI Terra (Version 4.0.1). The DJI Terra software uses the recorded images during processing to colorize the point cloud. The coordinate system in the software was set to North America Datum (NAD83)/UTM Zone 14N for the horizontal datum and Canadian Geodetic Vertical Datum 2013 (CGVD2013) for the vertical datum, which matches the system used during data capture with the LiDAR sensor. One of the software's features was utilized to merge five separate missions into a single mission. Before processing, 12 surveyed GCPs were imported into the software for georeferencing and to achieve more accurate point cloud generation. All GCPs were surveyed using the RTK-GNSS base and rover equipment.

In the next step, the desired point cloud density had to be decided. The maximum point cloud density that could be generated from the captured data in the mentioned configuration was approximately 360 points/m^2 (DJI, 2023), resulting in a huge LAS file that could not be imported into third-party software due to the associated heavy computational requirements. DJI Terra offers three point-cloud sampling options defined by the proportion of points used in point cloud generation: high (100%), medium (25%), and low (6.25%). Given the total number of captured points, the medium setting was expected to produce computationally heavy datasets. Consequently, the low setting (6.25%) was adopted, reducing the point-cloud density to approximately 23 points/m^2 and yielding a more manageable output for processing and analysis. Next, the point cloud effective distance range feature was used to eliminate noise caused by fog and moisture from the processed data. Using this feature, only returns acquired within a specified sensor-to-target distance were retained for subsequent analysis. As mentioned earlier, the surveying mission at DR07 was conducted at 100 m altitude, and after processing, some noise was detected in the point cloud. Consequently, this dataset was reprocessed by adjusting the effective distance range of the point cloud to 30 m from the sensor, rather than 3 m. In other words, all data points within 30 m of the LiDAR were discarded. Doing this resulted in a cleaner point cloud with significantly less noise, as shown in Figure 10.

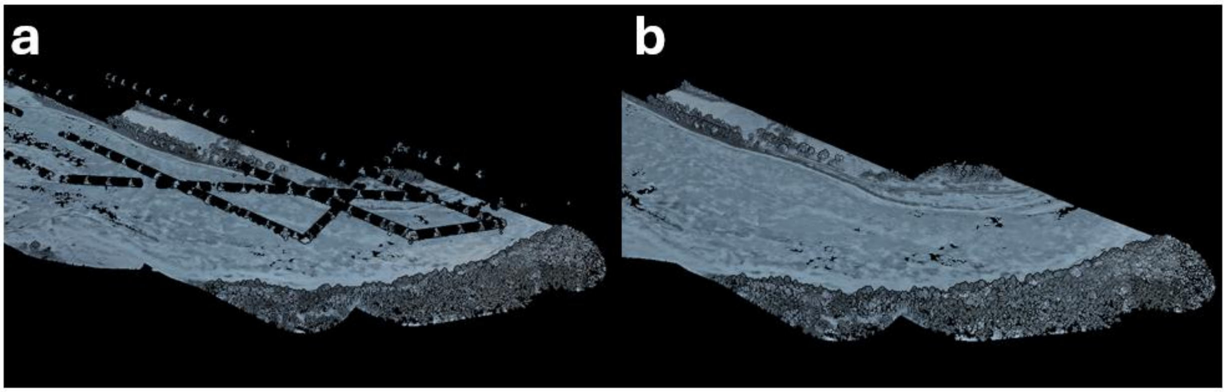

Figure 10. Adjusting the effective distance range of the point cloud from 30 m in (a) to 3 m in (b), resulting in the elimination of noise caused by moisture and fog.

The data processing time for these five missions combined was 10 hours. These five flights covered an area of 1.8 km², with an approximate width of 200 m (including riverbanks) and a length of 9 km. At this stage, the .las file (containing the captured points' coordinates) was used as an output from DJI Terra to import the point cloud into third-party software such as Agisoft Metashape to create a DEM. After importing the LAS file into Agisoft Metashape, the DEM generation command was employed to convert the point cloud into a DEM. This process can also be performed using other third-party software like QGIS or Pix4D. The complete procedure and steps needed to process the raw LiDAR data are summarized in Figure 11.

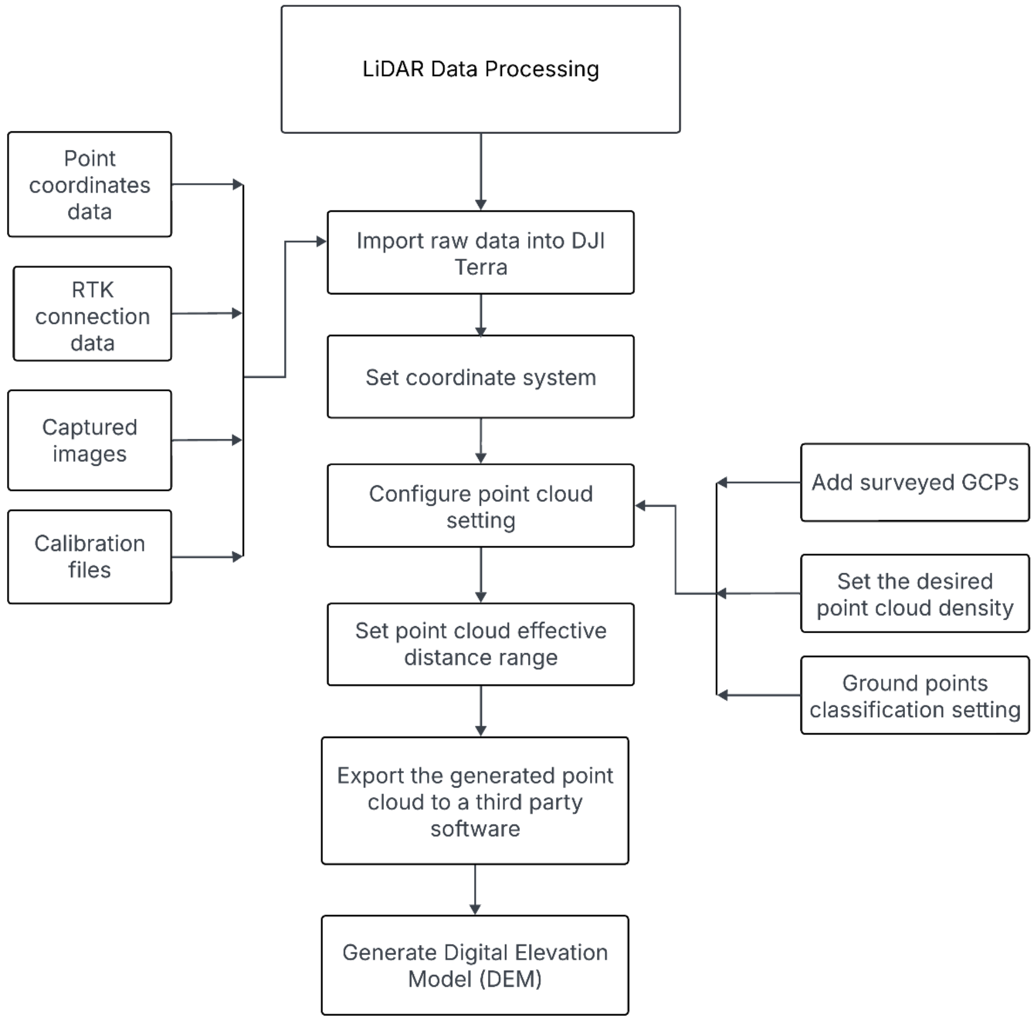

Figure 11. Flowchart illustrating the raw LiDAR data processing procedure

3.3 Results from Winter 2023/24

3.3.1 Generated Point Cloud

After the processing step, the first output of the DJI Terra software is the point cloud. This point cloud has a density of 23 points per square meter (41,860,000 in total), as shown in Figure 12.

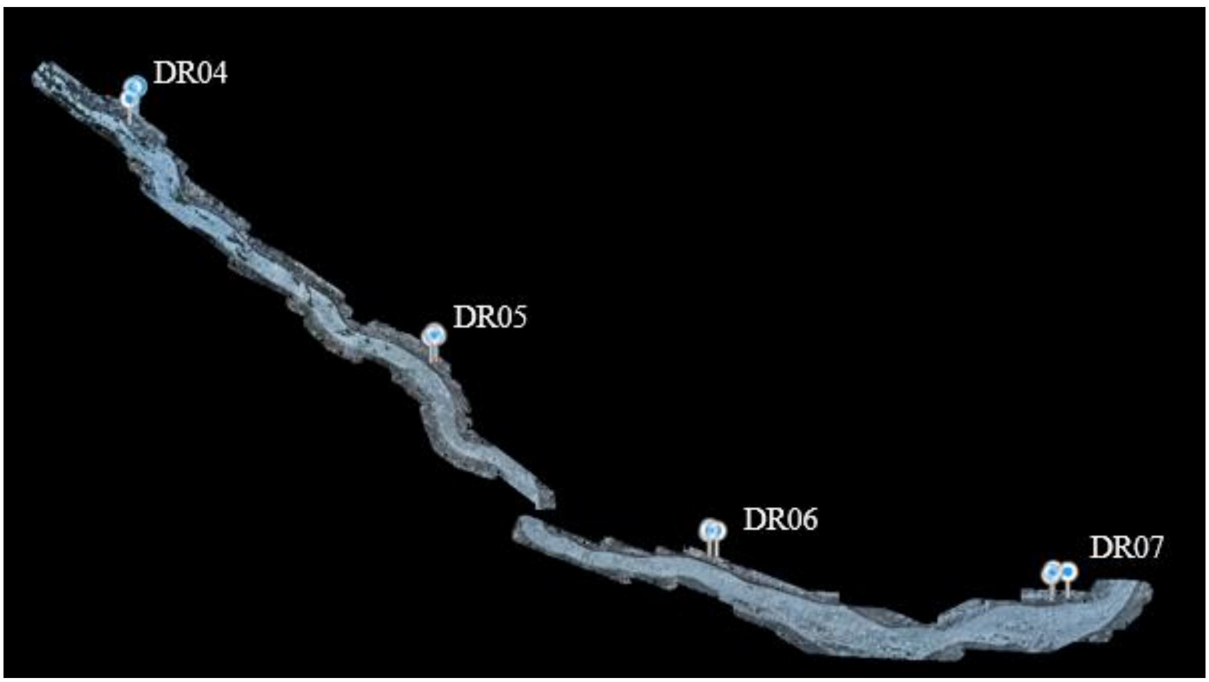

Figure 12. Reconstructed point cloud for a 9 km length of the Dauphin River in February 2024.

The generated point cloud was assessed for vertical accuracy using the surveyed ground control points (GCPs). The results are presented in Table 3. The root mean squared error (RMSE) between the reconstructed point cloud and the corresponding GCP elevations surveyed manually was calculated to be 0.022 m, indicating both the reliability of the data collection method and the high vertical accuracy of the point cloud. In section 3.3.2, the vertical accuracy of the resulting digital elevation model (DEM) was assessed and validated using the 18 top-of-ice elevation points collected during the fieldwork described in section 2.4.

Table 3. Vertical accuracy assessment of the reconstructed point cloud to surveyed GCPs.

Site	GCP #	GCP altitude (m)	Reconstruction altitude (m)	Altitude Difference (m)
DRO4	1	234.69	234.700	-0.010
	2	234.72	234.753	-0.033
	3	232.36	232.366	-0.006
DR05	1	234.76	234.769	-0.009
	2	234.6	234.602	-0.002
	3	227.76	227.797	-0.037
DR06	1	230.84	230.839	0.001
	2	231.16	231.129	0.031
	3	224.97	224.934	0.036
DR07	1	219.41	219.405	0.005
	2	224.59	224.615	-0.025
	3	219.82	219.817	0.003
			RMSE	**0.022**

3.3.2 Digital Elevation Model (DEM)

After importing the generated point cloud from the previous section into Agisoft Metashape software, the point cloud was converted into a DEM with a resolution of 0.5 m/pixel. This DEM was created from the entire surveyed area, including the vegetation near the banks, and is shown in Figure 13.

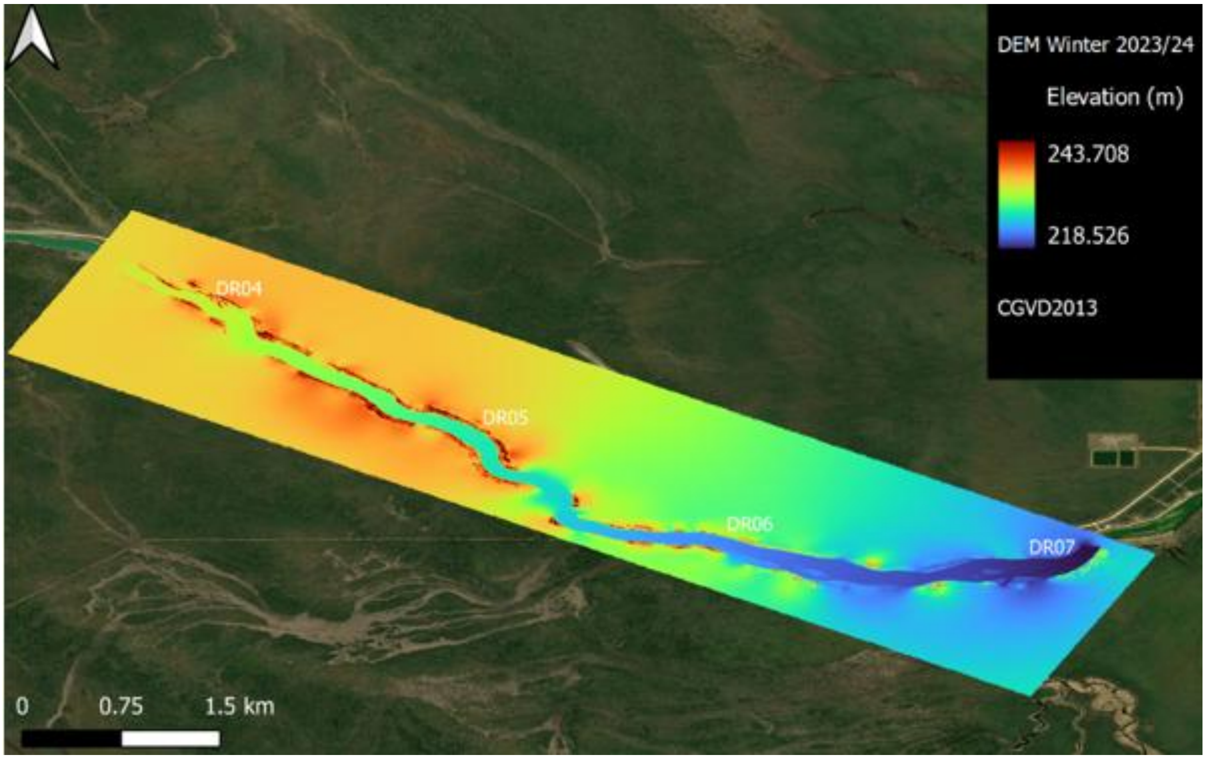

Figure 13. The generated DEM for the winter of 2023/24 for a 9 km length of the Dauphin River.

The elevation range of the original DEM was quite broad, capturing features such as tree canopies and riverbanks that are not relevant to this study. To focus the analysis, the river section of the DEM was cropped and extracted. On this cropped DEM, the coordinates of the 18 top-of-ice elevation points surveyed in Section 2.4 were overlaid to assess the vertical accuracy of the model. Figure 14 displays the cropped DEM with the manually surveyed points. Additionally, Table 4 presents a comparison between the DEM-extracted elevations and the manually surveyed values, including the calculated root mean squared error (RMSE).

The resulting RMSE was found to be less than 3.5 cm, indicating a high level of vertical accuracy. This result provides strong evidence that the DEM is suitable for post-processing applications related to monitoring river ice parameters.

Figure 14. Clipped DEM of Winter 2023/24 with 18 top-of-ice elevation points used for accuracy validation.

Table 4. Vertical accuracy assessment of the generated DEM using 18 top-of-ice elevation manually surveyed points.

Site	Points	Surveyed Elevation (m)	DEM Elevation (m)	Error (m)
DR07	top-ice-1	219.313	219.359	-0.046
	top-ice-2	219.464	219.451	0.013
	top-ice-3	219.512	219.574	-0.062
	top-ice-4	219.621	219.649	-0.028
	top-ice-5	219.566	219.614	-0.048
	top-ice-6	219.628	219.633	-0.005
	top-ice-7	219.708	219.734	-0.026
	top-ice-8	219.75	219.782	-0.032
	top-ice-9	219.724	219.781	-0.057
	top-ice-10	219.833	219.866	-0.033
	top-ice-11	219.826	219.879	-0.053
	top-ice-12	219.924	219.961	-0.037
DR06	top-ice-13	224.966	224.94	0.026
	top-ice-14	224.301	224.28	0.021
DR05	top-ice-15	227.634	227.658	-0.024
DR04	top-ice-16	232.167	232.1678	-0.0008
	top-ice-17	232.352	232.333	0.019
	top-ice-18	232.459	232.441	0.018
			RMSE	**0.0348**

3.4 Field Accuracy Tests

In the summer of 2024, an additional aerial survey using the DJI L2 LiDAR sensor was conducted to investigate the impact of various parameters on data quality, specifically focusing on vertical accuracy. The parameters examined included the number of GCPs used in processing, the point cloud density, and the flight altitude.

The guidelines outlined by the American Society for Photogrammetry and Remote Sensing (ASPRS, 2023) were followed to evaluate the vertical accuracy of the DJI Zenmuse L2 LiDAR system. ASPRS provides a standardized approach and equation for assessing the accuracy of geospatial products, accounting for potential errors originating from both the LiDAR sensor and the GNSS equipment used to collect the validation checkpoints. This methodology ensures a comprehensive evaluation of the system's performance under real-world conditions. Equation 5 calculates the RMSE error of the aerial survey by accounting for the combined contributions of errors from both the surveyed checkpoints and GCPs, as well as the error associated with the generated DEM.

Equation 5 $$Vertical\ Product\ Accuracy\ (RMSE_V) = \sqrt{{RMSE_{V1}}^2 + {RMSE_{V2}}^2}$$

In Equation 5, $RMSE_{V1}$ represents the vertical accuracy of the RTK-GNSS base and rover system used in this study, as discussed in Section 2.2.2. This system achieved an average vertical accuracy of 0.016 m, which is the value adopted for $RMSE_{V1}$in this assessment. $RMSE_{V2}$ corresponds to the actual elevation differences between the measured GCPs/checkpoints and the elevations extracted from the DEM. Combining these two RMSE components provides a more comprehensive representation of the overall vertical accuracy of the aerial survey.

This fieldwork was carried out at River’s Edge Nursery in La Barrière, Manitoba, and the results served as a foundation for planning the winter 2024/25 field campaign at the Dauphin River. During this survey, six GCP targets were established based on triangulation principles. These targets were used in different combinations to evaluate how the number of GCPs affects the accuracy of the resulting digital elevation model (DEM). Additionally, two separate flights were conducted at altitudes of 40 m and 100 m to assess how flight altitude influences vertical accuracy. According to DJI (2023), flying at a lower altitude increases the number of captured points per square metre on the ground, resulting in a higher point cloud density. However, the goal of this exercise was to empirically test how this translates into differences in vertical accuracy in our specific study context. It should be noted that in all of the following assessments, the RPA maintained a stable RTK connection with the base station.

3.4.1 Effect of GCP Number

To evaluate the effectiveness of the number of GCPs used in the processing step, the captured dataset was divided into three groups. These groups consist of having three GCPs, only one GCP, and no GCP in the processing step. To achieve this, the raw captured data at a flight altitude of 100 m was processed three times by varying the number of imported GCPs. In each mission, the imported GCP(s) served as calibration points, and the remaining surveyed targets were used as validation. Table 5 illustrates the impact of varying the number of GCPs on the processing of raw LiDAR data.

Table 5. Evaluating the Impact of GCP Number on Vertical Accuracy of the Generated DEM.

Dataset #	# of imported GCPs	$RMSE_{V1}$ (m)	$RMSE_{V2}$ (m)	$RMSE_{V}$ (m)
1	0	0.016	0.734	**0.734**
2	1	0.016	0.030	**0.034**
3	3	0.016	0.030	**0.034**

As shown in Table 5, incorporating at least one GCP is essential to achieve an acceptable vertical offset. When no GCP was used during processing, the vertical offset was approximately 0.73 m. However, the analysis indicates that using more than one GCP does not improve vertical accuracy. A single GCP, in combination with the RPA's RTK positioning system, is sufficient to maintain accuracy within an acceptable range. This finding is particularly valuable for field operations conducted during winter under harsh conditions, where minimizing the number of GCPs can streamline the survey process and reduce the risk of injury during fieldwork. In terms of vertical accuracy of airborne LiDAR, Kim et al. (2022) reported an RMSE of 0.017 m by evaluating the point cloud using amorphous objects. Similarly, Buffington et al. (2016) demonstrated that, after applying statistical correction using multispectral airborne imagery in tidal marshes, an RMSE of 0.072 m could be achieved. These studies indicate that the RMSE values obtained in our research fall within an expected and acceptable range.

3.4.2 Point Cloud Density and Flight Altitude

Another set of important parameters affecting LiDAR data quality are point cloud density and flight altitude, which are closely related. Flying at a lower altitude results in a higher number of captured points, thereby increasing point cloud density. As previously discussed, the desired density can also be adjusted during processing by selecting the percentage of points used to generate the final point cloud. Figure 15 illustrates the difference between two point clouds captured at the same flight altitude, Figure 15a processed with a high-density configuration and Figure 15b with a low-density configuration.

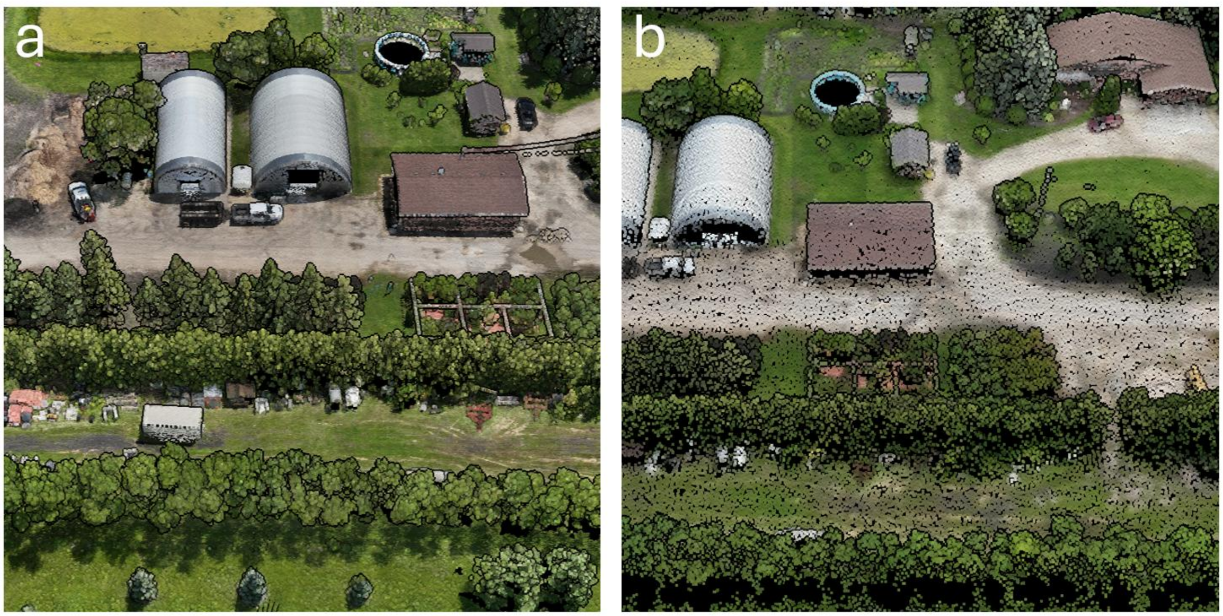

Figure 15. A visual illustration of the difference between high and low-density point clouds. (a) high-resolution point cloud; (b) generated point cloud using the low-resolution setting.

To assess the combined effect of these parameters, two flight altitudes, 40 m and 100 m, were each processed with both high and low point cloud densities (i.e., high density point cloud refers to using 100% of the captured points, while low density refers to using only 6.25% of them), creating four distinct scenarios. Table 6 presents the $RMSE_v$ for each case, representing the final vertical accuracy achieved in each configuration.

Table 6. Comparison of vertical accuracy under different scenarios by varying flight altitude and point cloud density.

Scenario	Flight Altitude (m)	Point cloud density level	$RMSE_v$
1	100	High	0.040
2	100	Low	0.054
3	40	High	0.024
4	40	Low	0.036

Based on Table 6 , a comparison between scenarios 1 and 3, as well as scenarios 2 and 4, indicates that reducing the flight altitude leads to improved vertical accuracy. Additionally, comparing scenarios 1 to 2 and 3 to 4 shows that higher point cloud densities result in slightly better $RMSE_v$ values. While this trend is evident, it is important to note that increased point cloud density does not inherently guarantee improved vertical accuracy. Instead, higher density increases the likelihood that LiDAR points closely coincide with surveyed checkpoints or GCPs, which can enhance validation results. However, for applications that do not require extremely high spatial detail, lower-density point clouds may still achieve acceptable accuracy.

The results of the field accuracy tests provided valuable insight into how to plan the aerial survey of the river for the winter 2024/25 campaign. The survey plan and its connection to the findings from the accuracy tests are discussed in the next section.

3.5 Winter 2024/25

Based on the findings from the field accuracy tests, it was concluded that a single GCP is sufficient to maintain acceptable vertical accuracy. In terms of flight altitude and point cloud density, the results indicated that a 100 m flight altitude offers a reasonable level of accuracy. However, it may not capture fine surface details due to reduced point density. Given the objectives of this study, evaluating ice thickness and surface roughness using airborne LiDAR, the winter 2023/24 flight mission was planned to be replicated at the same altitude (100 m); however, in the 2024/25 study year, the reach covered extended only from DR05 to DR07, excluding DR04, and thus represented a shorter section of the river. Conducting the survey at a lower altitude was not practical due to time constraints and battery limitations in cold weather. Moreover, since the goal was to obtain a reliable estimate of top-of-ice elevation rather than capture fine-scale surface features, the 100 m altitude configuration was deemed appropriate.

For the surface ice roughness analysis, three separate LiDAR missions were conducted at site DR06, which was identified as the most suitable location due to its tendency to experience rough ice jams. These missions were flown at a low altitude using three different RPA speeds, from high to low, to capture varying levels of surface detail. Additionally, a separate survey using a photogrammetry payload was conducted to facilitate a direct comparison between photogrammetry-based and LiDAR-based surface roughness assessments. It should be noted that eight GCPs were placed and surveyed at site DR06 because of the requirement for a larger number of GCPs for the photogrammetry survey. The results of the aerial surveys from winter 2023/24 and winter 2024/25 will be thoroughly discussed in Chapters Chapter 4 and Chapter 5.

Chapter 4 Ice Thickness Estimation Using LiDAR Data

This research addresses a fundamental aspect of ice mechanics that occurs following the formation of a stationary ice jam. As described by Lindenschmidt (2020), when water levels rise, hinge cracks often develop near the riverbanks due to the limited flexural strength of the ice, which prevents it from bending in response to changes in water surface elevation. These cracks result in the detachment of the ice cover from the banks, allowing the ice to float freely in a state of hydrostatic equilibrium, rather than remaining fixed and creating pressurized flow conditions. This floating behavior enables the estimation of ice thickness using principles of buoyancy.

To apply this method, simultaneous measurements of the top-of-ice elevation and water surface elevation are required. Assuming a typical ice density with a specific gravity of 0.92, it can be inferred that approximately 92% of the ice thickness lies below the water surface. Based on this relationship, the total ice thickness can be back-calculated using Equation 6. It is important to note that this method is only valid under the assumption that the ice cover is floating in hydrostatic equilibrium.

Equation 6

$$T_i = \frac{T_{oi} - WSE}{1 - SG_i}$$

In Equation 6, T_i represents the ice thickness, defined as the vertical distance between the top and bottom surfaces of the ice cover. T_{oi} denotes the top-of-ice elevation, which refers to the height of the ice surface relative to a known vertical datum (i.e., CGVD2013). *WSE* denotes the elevation of the phreatic surface, which may either be located slightly below the ice cover or may be visible at specific locations where the surface ice concentration is less than 100%, also referenced to the same datum. Lastly, SG_i is the specific gravity of ice, defined as the ratio of the density of ice to the density of water. For freshwater ice, a typical value of 0.92 is commonly assumed.

4.1 Top-of-Ice Elevation

Top-of-ice elevation is a crucial parameter to know when monitoring river ice processes such as ice jam formation. Researchers can use this data to estimate ice thickness or to calibrate hydraulic models. Traditionally, research teams collected top-of-ice elevation points near the riverbanks using manual survey methods. However, this approach was often dangerous and time-consuming due to harsh winter conditions. Another limitation of these traditional methods is the uncertainty introduced by the irregularity of the ice surface, particularly in areas affected by ice jams, as illustrated in Figure 16. Since the ice surface is not uniform, selecting a single point on top of the ice may not accurately represent the actual top-of-ice elevation for that location. Additionally, the number of surveyed points was limited due to the labor-intensive nature of the work. As a result, researchers often had to rely on sparse, discrete datasets that carried a degree of uncertainty and were difficult to collect.

Figure 16. Ice jam formation at site DR05A, illustrating the non-uniformity of the top-of-ice elevation.

An alternative method for surveying river ice is using remote sensing tools like RPA-based photogrammetry or LiDAR-based surveying. In 3.2, the processing of raw LiDAR data and the generation of DEMs were thoroughly discussed. To move forward with the analysis, the focus now shifts to the post-processing steps required to extract relevant information from the generated DEMs. All post-processing was conducted using QGIS, an open-source geographic information system software, for the winter seasons of 2023/24 and 2024/25, approximately 9 km and 7 km of the river length were surveyed, respectively, and used to generate the DEMs covering the entire study extent. Compared to traditional methods, this type of survey offers several advantages. It is significantly less labor-intensive and reduces the risk of injury to the research team during fieldwork, particularly given the hazardous conditions of winter surveys near riverbanks. At the same time, the captured dataset provides highly detailed information about the surveyed area, allowing for the extraction of continuous datasets from the DEMs. Moreover, access to a complete dataset enables the application of advanced techniques to substantially reduce uncertainty. The following section outlines the post-processing steps used to extract a continuous top-of-ice elevation profile.

4.1.1 Extraction of Top-of-ice Elevation from DEMs

The first step in extracting top-of-ice elevation from the DEMs is to import the generated models into QGIS software. Two approaches were defined to extract the elevation data. The first, and simpler, method involves drawing a centerline along the river path and using the Profile Tool plugin in QGIS to extract elevation values along this line. This approach already offers several advantages over traditional survey methods: it provides a continuous, high-resolution dataset and allows data extraction from the middle of the river, which is typically inaccessible using manual surveying techniques.

This is particularly important because ice near the banks is often border ice, which forms thermally and tends to be thinner and more uniform. In contrast, ice in the middle of the river, especially within ice jams, is formed mechanically through accumulation and compaction of ice floes, and can reach thicknesses of several meters. Additionally, bank ice may be subjected to different heat flux conditions due to shading from nearby vegetation, which affects sunlight exposure and melting rates. Furthermore, as observed in the research by Wazney et al. (2018), ice chunks near the banks can become grounded and pushed up further along the banks, resulting in unusually high top-of-ice elevations. These localized elevations may not accurately represent the actual top-of-ice elevation and could introduce errors if used for hydraulic model calibration.

Although the centerline-based approach offers several advantages over traditional survey methods, a second approach was introduced to further reduce the uncertainty associated with using a single elevation value to represent each cross-section, especially given the non-uniform surface characteristics of ice jams. In this method, perpendicular transects were drawn at regular intervals (e.g., every 50 m) along the river, intersecting the centerline. Elevation data along each transect were then extracted from the DEM and averaged to represent the top-of-ice elevation at that specific cross-section. Each transect contains 100–200 elevation data points; therefore, averaging these points provides a more reliable estimate of the top-of-ice elevation at each cross-section. It significantly reduces the influence of localized anomalies or irregularities in the ice cover, thereby enhancing the overall accuracy and consistency of the top-of-ice elevation dataset. Figure 17 shows a detailed procedure for extracting top-of-ice data from DEMs using these two different approaches.

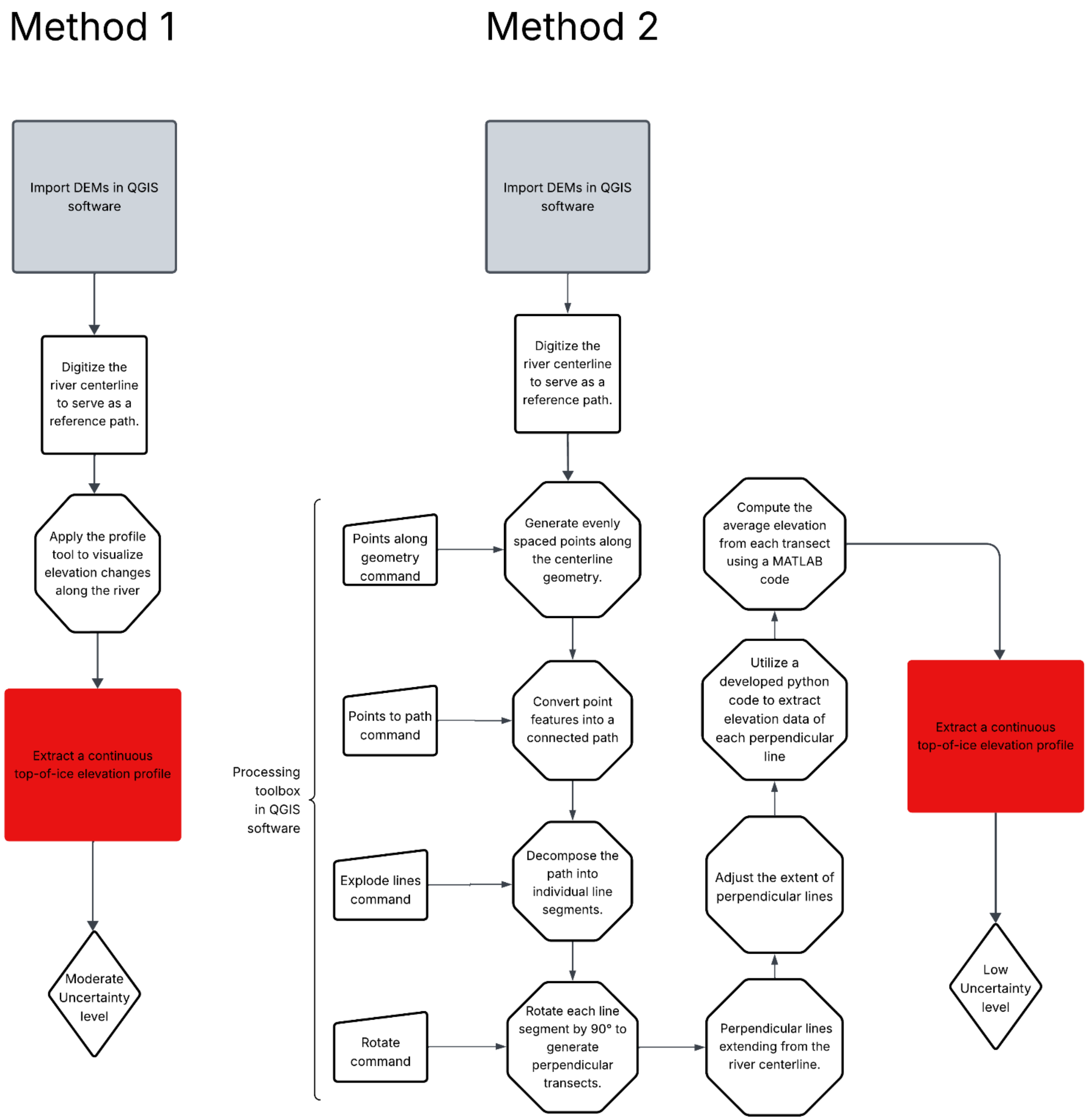

Figure 17. Flowchart illustrating two distinct methods for extracting the top-of-ice elevation profile

4.1.2 Top-of-ice elevation winter 2023/24 and winter 2024/25

By utilizing the first approach, a continuous top-of-ice elevation was extracted from the generated DEM for the winter 2023/24. Figure 18 illustrates the plotted dataset.

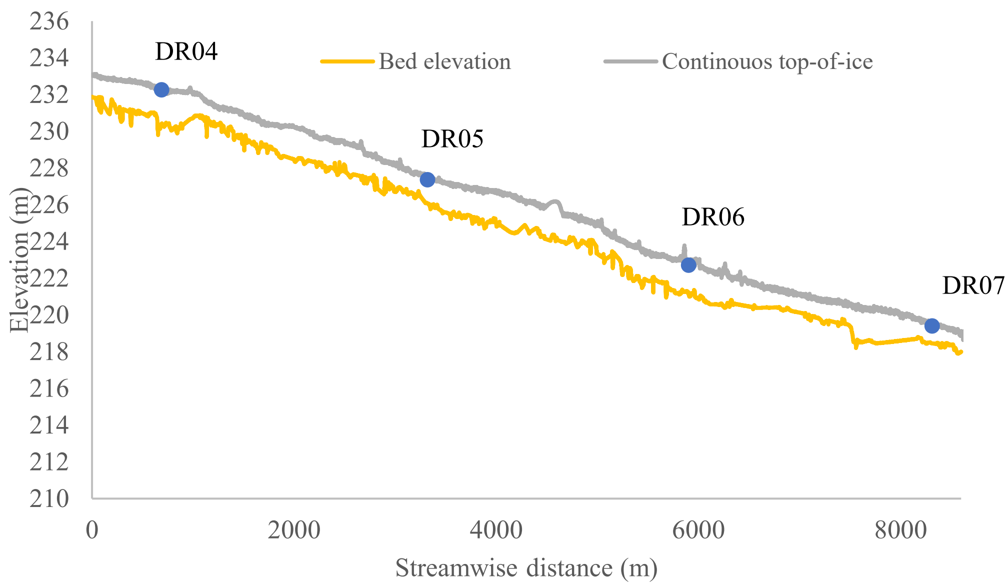

Figure 18. Continuous top-of-ice elevation profile for 9 km of the Dauphin River during winter 2023/24.

In Figure 18, the grey line shows the continuous top-of-ice elevation and the yellow line depicts the bed elevation of the Dauphin River. The yellow line represents the dataset from a bathymetric survey conducted by KGS Group in 2011. Given that the bathymetric survey was conducted approximately 14 years ago and the river is morphodynamically active, experiencing thick ice jams and anchor ice, the available bathymetric data may not accurately represent current bed elevations. Nevertheless, as this is the only dataset available, it is used herein.

Lindenschmidt et al. (2012) calibrated an RIVICE model for the lower Dauphin River using only three top-of-ice elevation points. Subsequently, Lindenschmidt et al. (2013) validated the same

RIVICE model for the same reach with just six WSE observations, reflecting limited field data availability. In contrast, the dataset presented in this study provides a continuous, high-resolution top-of-ice elevation profile with 26775 top-of-ice elevation points along a 9 km stretch of the Dauphin River, offering the most spatially detailed ice cover dataset to date in river ice engineering research. This comprehensive dataset addresses previous data gaps by enabling more robust calibration and validation of ice jam hydraulic models.

The second approach described in the previous section was applied to the DEM generated for the winter of 2024/25. Figure 19 shows the clipped DEM for that season, overlaid with the river centerline and a series of perpendicular transects spaced at 50 m intervals. As shown in the figure, several of the perpendicular lines were adjusted in length upstream of site DR07. This modification was necessary due to the presence of natural islands in that region, where ice chunks had become grounded. Extracting data from these areas could result in false top-of-ice elevation values. To avoid this, the lengths of the affected perpendicular lines were modified to prevent them from intersecting the grounded ice near the islands. In Figure 20, the top-of-ice elevation plotted is the one extracted and averaged using MATLAB code for winter 2024/25.

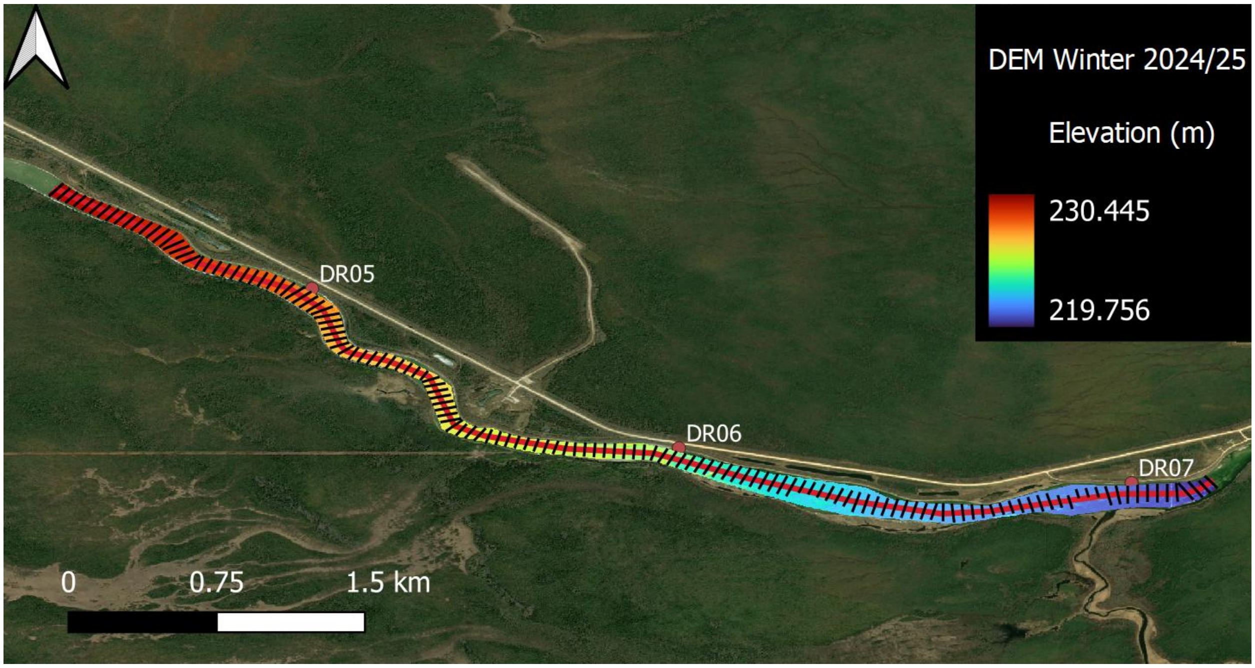

Figure 19. The generated DEM of the winter 2024/25 survey campaign was created by adding perpendicular lines over the DEM to extract data using the second approach.

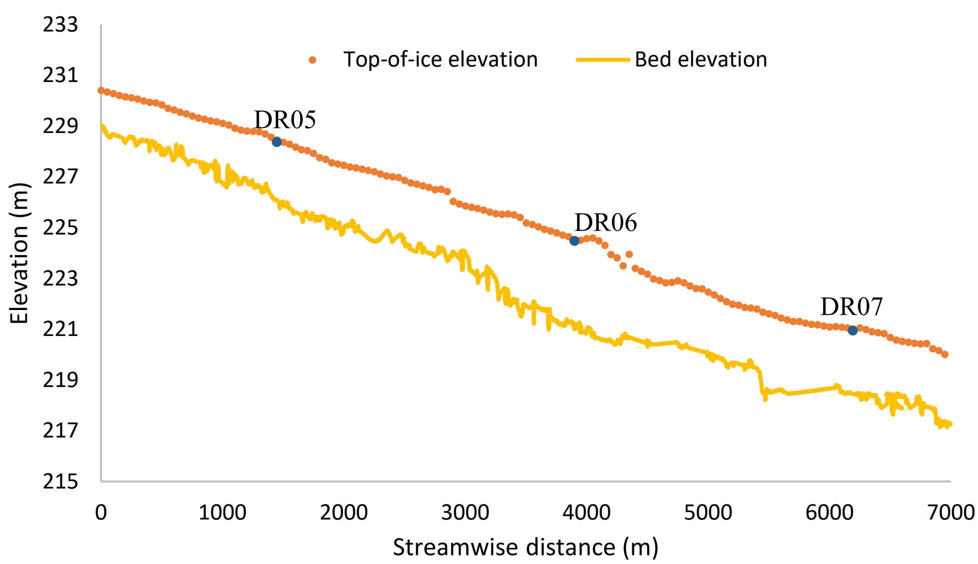

Figure 20. High-resolution top-of-ice elevation profile extracted using the second approach for 7 km of the Dauphin River during winter 2024/25.

4.2 Water Surface Extraction From DEM

Up to this point, a high-resolution top-of-ice elevation profile has been successfully extracted. To proceed with the methodology described earlier, a continuous water surface elevation (WSE) profile is required for the same time in order to derive a continuous ice thickness profile. However, measuring WSE during the freeze-up season is highly challenging, if not impossible, due to the full ice coverage of the river, which prevents direct access to the water surface for manual measurements. Furthermore, the presence of a rough ice cover makes the task of manually drilling auger holes to facilitate water surface elevation measurement quite challenging. As outlined in Section 2.2.1, level loggers were installed prior to the freeze-up for both the 2023/24 and 2024/25 winters. These loggers continuously recorded water level data throughout the freeze-up period. Despite this, only four level loggers were deployed across the entire study area, resulting in a spatially sparse dataset. Moreover, due to the complex winter hydraulics, affected by factors such as ice roughness, ice thickness, and variable topography, including sudden changes in riverbed slope, it is not feasible to accurately interpolate water surface elevations using a simple linear regression between these four points. Such an approach would fail to capture the true variability of the WSE profile along the river under ice-covered conditions.

To obtain the water surface elevation profile using the available aerial survey data, a specific methodology was developed. Upon reviewing the aerial images captured by the LiDAR sensor during the winter of 2023/24, it was observed that several open water sections existed along the river stretch from site DR04 to DR07. Although the LiDAR sensor used in this study is not capable of capturing returns from open water surfaces, it was able to detect fine details adjacent to these areas. In many of these sections, the ice cover was thin and fragile, and the corresponding top-of-ice elevation points are considered to be reliable indicators of the actual water surface elevation.

Figure 21 presents aerial imagery highlighting some of these open water sections and thin ice cover observed during the winter 2023/24 survey.

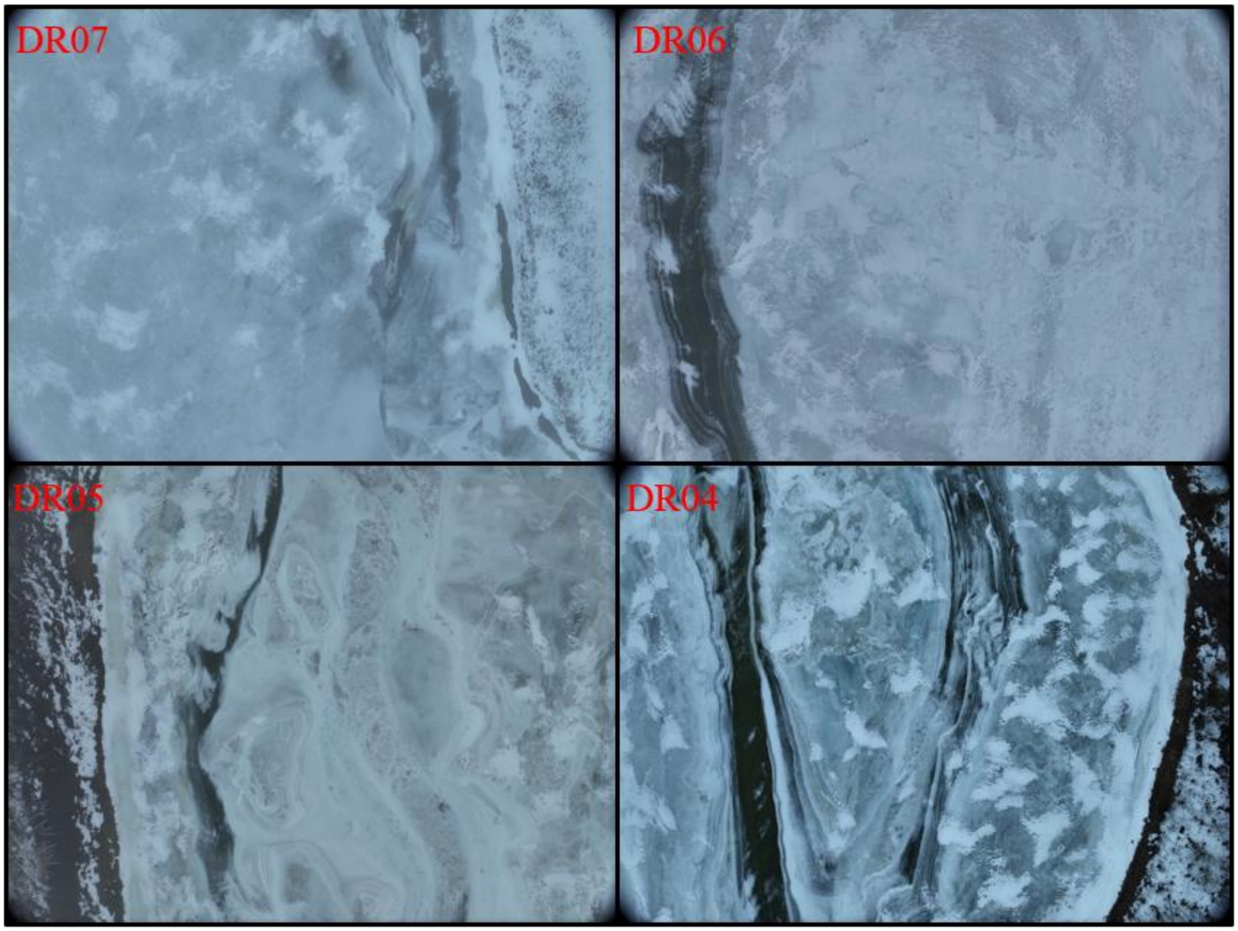

Figure 21. Presence of open water sections throughout the entire study area.

Given the presence of open water sections and thin ice cover throughout the surveyed area, the perpendicular-transect method used for detailed top-of-ice profiling was adapted to derive water-surface elevation (WSE). For each transect, the full elevation dataset was extracted, and the minimum elevation was taken as the representative WSE at that cross-section. This method allowed us to estimate a continuous water surface elevation profile for the study site. It is worth noting that during the LiDAR survey conducted in winter 2023/24, there was little to no snow cover on the ice surface, which enhanced the quality and clarity of the captured data. However, this method assumes that the lowest elevation points correspond to the water surface; therefore, it requires validation.

To validate the extracted water surface elevations, comparisons were made against the measurements recorded by the level loggers deployed at fixed locations. This required identifying the date and time of the LiDAR survey and matching it with the corresponding logger data. Table 6 presents a comparison between the water surface elevations extracted from the DEM and the recorded values from the level loggers at the corresponding locations and times.

Table 7. Comparison between the water surface elevations extracted from the level loggers and the DEM winter 2023/24.

Time	Site	Level Logger elevation (m)	DEM elevation (m)	Absolute error (m)
Feb 5 @11:00 am	DR07	219.4	219.420	-0.020
Feb 5 @12:45 pm	DR06	222.71	222.691	0.019
Feb 5 @ 02:15 pm	DR05	227.36	227.345	0.015
Feb 5 @ 04:00 pm	DR04	232.25	232.193	0.057

Table 7 shows that the validation results are acceptable, with a maximum absolute error of less than 6 cm. It is important to note that the LiDAR-derived water surface elevations inherently include a vertical uncertainty associated with the airborne LiDAR system, as discussed in 3.4. Considering this, the validation results demonstrate excellent agreement, indicating that the extracted water surface profile is of high quality and suitable for further analysis.

A similar method was applied to the dataset from the winter of 2024/25 to extract the water surface elevation from the generated DEM for that year. However, the conditions during the winter

2024/25 survey differed notably from those in the previous year. Significantly fewer open-water sections were captured by the LiDAR. On December 11, 2024, the date of the LiDAR survey, the ice cover was partially obscured by a few centimeters of snow (Figure 22).

Figure 22. Trail camera images show entirely ice-covered areas with no visible open-water sections and a continuous snow cover at sites DR06 (top image) and DR05 (bottom image).

These conditions contributed to an increased error between the water surface elevation values extracted from the DEM and those recorded by the level loggers. The presence of snow, even on thin or fragile ice, resulted in elevations higher than the actual water surface. Additionally, in some locations, the river was covered by a thick, continuous ice sheet from bank to bank, making it impossible for the previous method to capture an accurate representation of the water surface.

Table 8 presents the absolute errors between the water surface elevations derived from the DEM and those measured by the level loggers for winter 2024/25, highlighting the reduced accuracy under these more challenging conditions.

Table 8. Comparison between the water surface elevations extracted from the level loggers and the DEM during winter 2024/25.

Date & Time	Site	Level Logger elevation (m)	DEM elevation (m)	Absolute error (m)
Dec 11 @10:45 am	DR07	220.347	220.434	-0.183
Dec 11 @11:30 am	DR06	223.72	223.811	-0.095
Dec 11 @02:00 pm	DR05	227.79	228.120	-0.37

All water surface elevations extracted from the DEM for winter 2024/25 were found to be consistently higher than the corresponding values recorded by the level loggers. This indicates a systematic overestimation, likely due to the presence of snow and ice layers in the entire sections used to extract water surface elevation. To address this issue and improve the accuracy of the extracted data, the methodology was refined.

A Digital Orthophoto Map (DOM) was generated and overlaid on the DEM to enable visual identification of open water sections. By manually selecting these verified open water areas, more reliable water surface elevation points could be extracted. A total of 20 perpendicular transects were drawn across the identified open water sections, and the water surface elevations were extracted at the intersection points between these transects and the open water areas. Figure 23 shows the generated DOM with the drawn transects over the identified open water sections, along with a zoomed-in view near site DR06 for further detail.

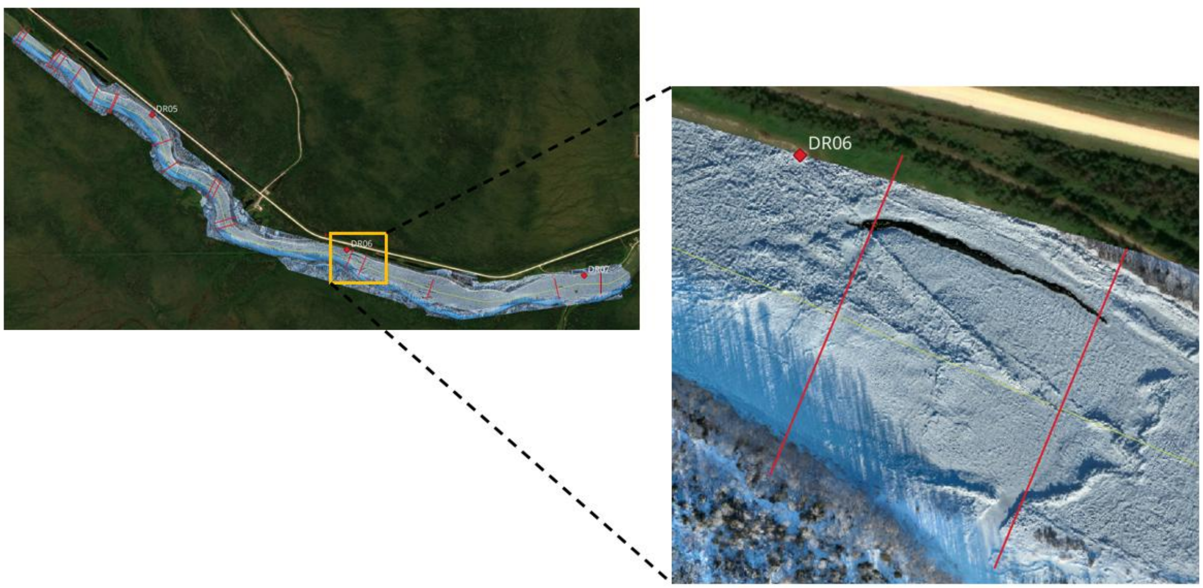

Figure 23. The generated DOM from LiDAR data is overlaid with drawn transects over the open water sections in QGIS.

Subsequently, interpolation was applied between the verified points to construct a more accurate and continuous water surface elevation profile. Available level logger data was used again to validate the estimation of the water surface profile.

Figure 24 presents the continuous water surface elevation profile extracted from the DEM using the initial and refined methodology for winter 2024/25. Validation against level logger data at sites

DR07, DR06, and DR05 shows a reduction in absolute error to -0.068 m, -0.041 m, and -0.309 m, respectively. Although the absolute error was reduced through the refined methodology, it remains relatively high at site DR05 between the measured and estimated water levels. Figure 25 presents the zoomed-in DOM of site DR05. As illustrated, no open-water sections were located within 300 m of the level logger at this site. Consequently, the estimated WSE at DR05 was derived through linear interpolation between the estimated WSE values at the upstream and downstream open-water sections. Given the bathymetry of the Dauphin River at DR05, a sudden drop in bed elevation occurs just downstream of the site, which may contribute to a rapid decrease in water level near this location. However, this feature was not captured in the interpolation process, as it lies within the interpolation range. The lack of data points within this range could therefore be a contributing factor to the relatively high error observed at DR05. In the next section, the improved WSP dataset will be used to estimate the ice thickness profile for winter 2024/25.

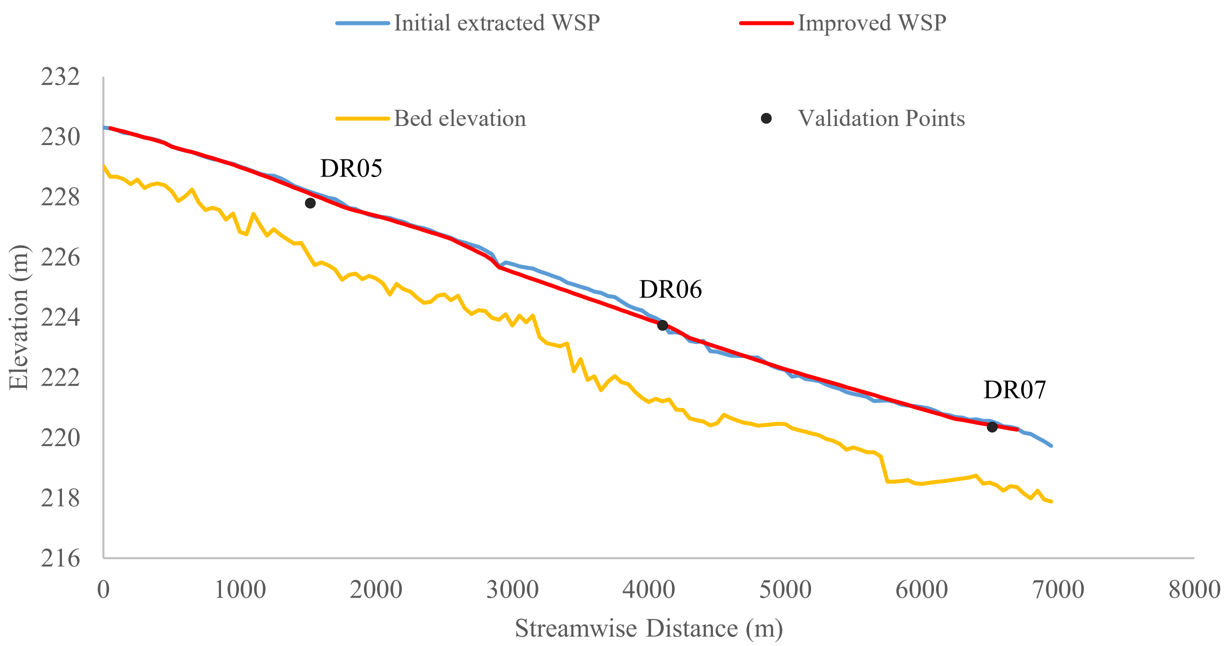

Figure 24. The comparison of extracted WSP using the initial and improved methods for Winter 2024/25.

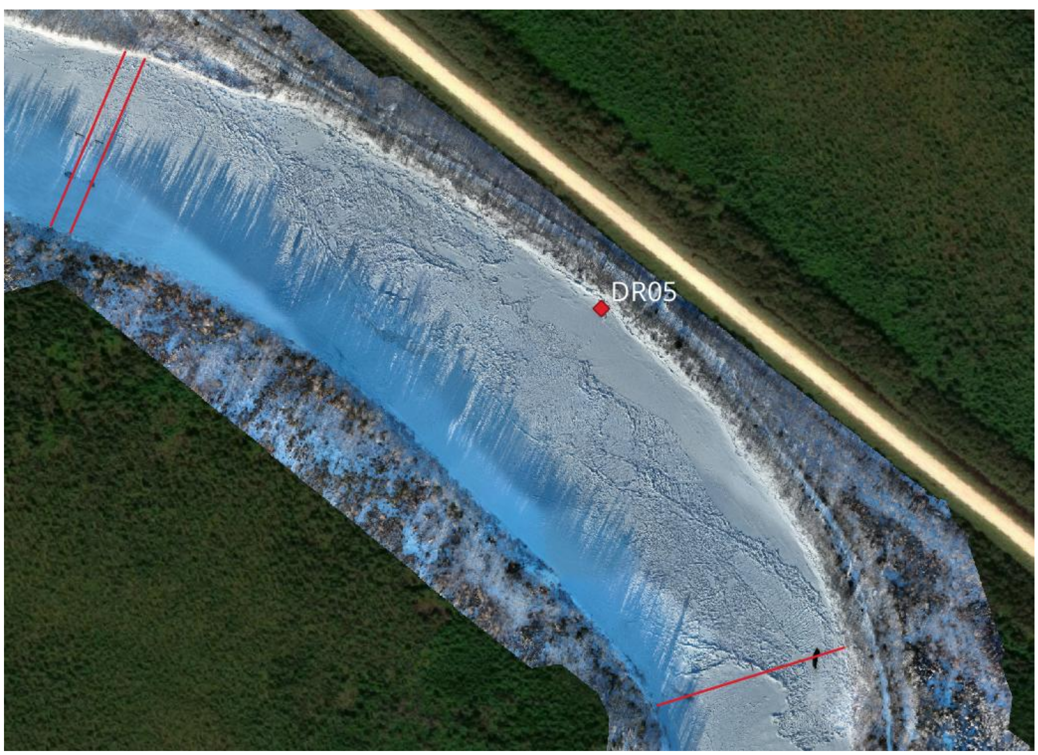

Figure 25. Zoomed DOM of site DR05 illustrating the absence of open-water sections within 300 m upstream and downstream of the site.

4.3 Ice Thickness Estimation

4.3.1 Winter 2023/24

In the previous steps, continuous top-of-ice elevation and water surface elevation profiles were successfully extracted from the DEM for a 9 km stretch of the Dauphin River. Both datasets were validated and found to be sufficiently accurate for use in ice thickness estimation. With these validated profiles, the principle of freeboard (i.e., Equation 6) can now be applied to estimate ice thickness along the entire surveyed reach. In this procedure, top-of-ice elevation and water surface elevation are available for each cross-section of the river. The difference between these two values represents approximately 8% of the total ice thickness, corresponding to the portion of the ice cover that lies above the water surface, based on the assumed specific gravity of ice of 0.92. Using this relationship, the total ice thickness can be calculated, allowing for the estimation of the bottom-of-ice elevation. Applying this method across all cross-sections results in a continuous ice thickness profile spanning approximately 9 km of the river. Figure 26 shows the plotted ice thickness profile along with the bed elevation profile. In this graph, the Interquartile Range (IQR) values of each perpendicular elevation profile were calculated to represent the corresponding surface roughness at each selected cross-section.

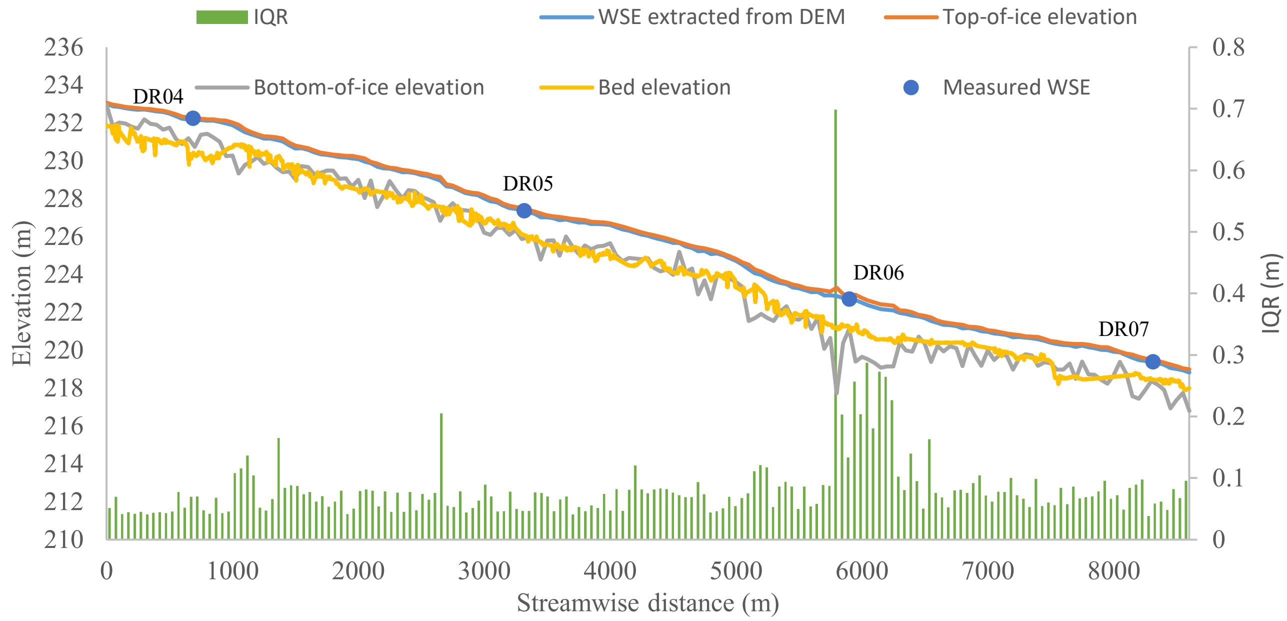

Figure 26. Continuous ice thickness profile of winter 2023/24 for 9 km of the Dauphin River.

Figure 26 presents the continuous ice thickness profile for the winter of 2023/24. In this graph, the grey line represents the bottom-of-ice elevation. At certain locations, this line falls below the riverbed elevation, which is physically impossible. This led to the conclusion that, in areas where the bottom-of-ice elevation is lower than the bed elevation, the ice has likely become grounded. This phenomenon is particularly evident at site DR06, a location historically known for forming thick and grounded ice jams (Wazney et al., 2019).

To differentiate between grounded and non-grounded conditions across various sites, the Interquartile Range (IQR) was calculated for each perpendicular elevation profile. The IQR, defined as the difference between the 75th and 25th percentiles of the elevation dataset, serves as a representative measure of surface roughness height. These IQR values are displayed on the right vertical axis of Figure 26. A clear correlation was observed between higher IQR values, indicating increased surface roughness, and the presence of grounding (i.e., when the bottom-of-ice lies below the bed elevation). Based on this finding, the ice thickness profile was revised by adjusting the bottom-of-ice elevation to match the bed elevation at locations where grounding was identified. The updated ice thickness profile is shown in Figure 27. In the updated plot, ice thickness is calculated by subtracting the bottom of the river from the top-of-ice elevation in areas where the ice jam is grounded. In other locations, where the ice is floating, ice thickness is determined by subtracting the bottom-of-ice elevation from the top-of-ice elevation.

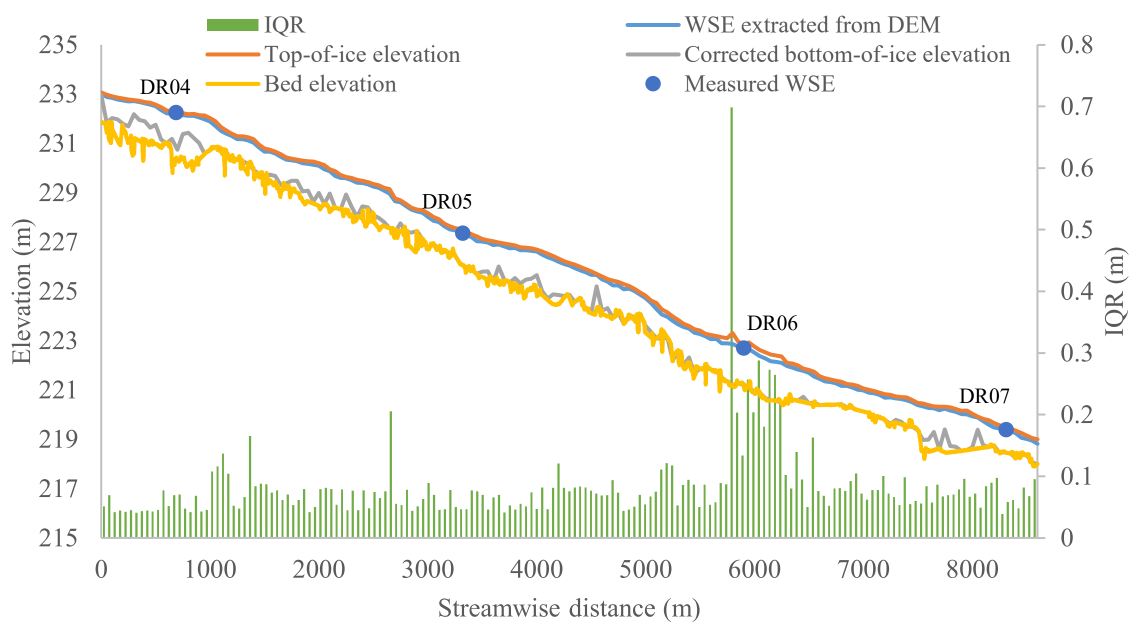

Figure 27. Corrected ice thickness profile for winter 2023/24, accompanied by ice surface IQR values representing roughness height at each cross-section.

Multiple factors influence ice jam grounding. One primary cause is the mechanical thickening of the ice jam, which occurs when large blocks of ice accumulate and compact within the channel. A typical indicator of this process is a rough ice surface, resulting from the chaotic collision and stacking of ice blocks. Grounding is also strongly influenced by riverbed topography. As shown in

Table 2, the Dauphin River is naturally a very shallow river, with an average open water depth of around 1 m throughout the study area. Consequently, grounding during the winter of 2023/24 was anticipated, since such limited depths within this river reach increase the likelihood of grounding. This observation reinforces the idea that grounding is governed by a combination of factors, including ice jam structure, river geometry, and local bathymetry.

4.3.2 Winter 2024/25

The same methodology was applied to the data captured during the winter of 2024/25 to estimate the ice thickness profile for that year. The main difference lay in the approach used to extract the water surface profile (WSP), which was adapted to account for different site conditions compared to the previous year, as discussed in Section 4.2. Figure 28 presents the resulting ice thickness profile for winter 2024/25. As shown in this plot, the grey line representing the bottom-of-ice elevation lies below the bed elevation throughout most of the surveyed reach, except upstream of site DR07. This is not unexpected, as the 2024/25 survey was limited to sites DR05 through DR07, excluding site DR04. These three sites have been historically recognized for the formation of thick ice jams. Additionally, the observed IQR values support the grounding assumption. In particular, site DR06 exhibited very high IQR values, indicating a significantly rough ice jam surface.

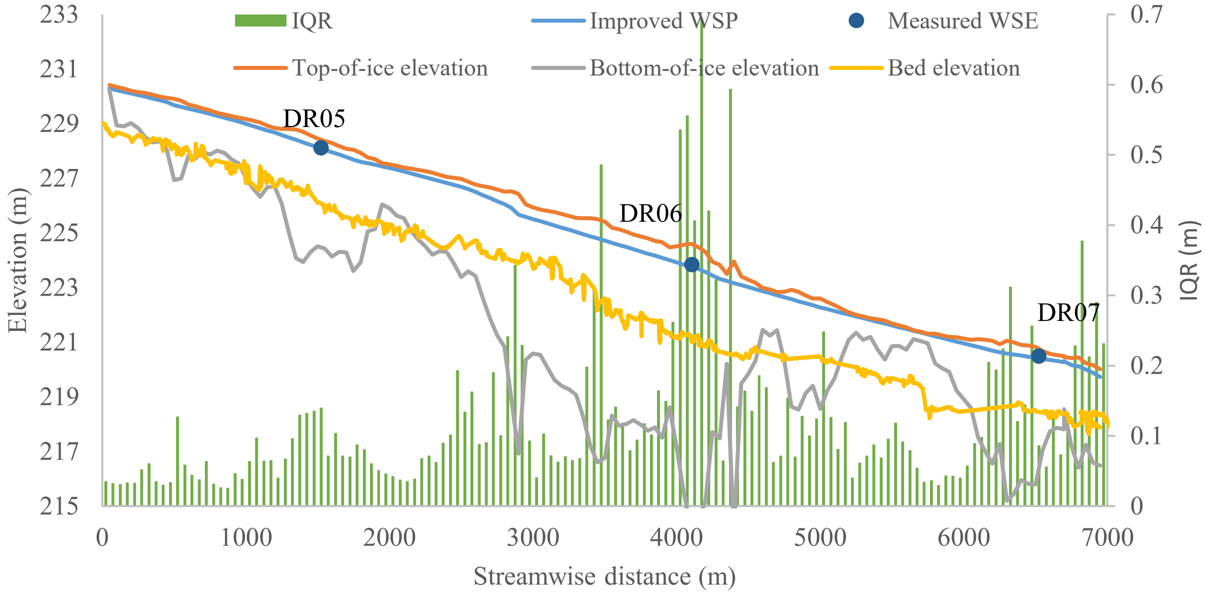

Figure 28. Continuous ice thickness profile of winter 2024/25 for 7 km of the Dauphin River.

As shown, in several areas, the estimated bottom-of-ice elevation falls below the riverbed elevation (indicated by the yellow line), which is physically unrealistic. This discrepancy suggests that the ice jam was grounded in those regions. Consequently, the bottom-of-ice elevation in these sections was adjusted to match the bed elevation, and a corrected ice thickness profile was produced, as illustrated in Figure 29.

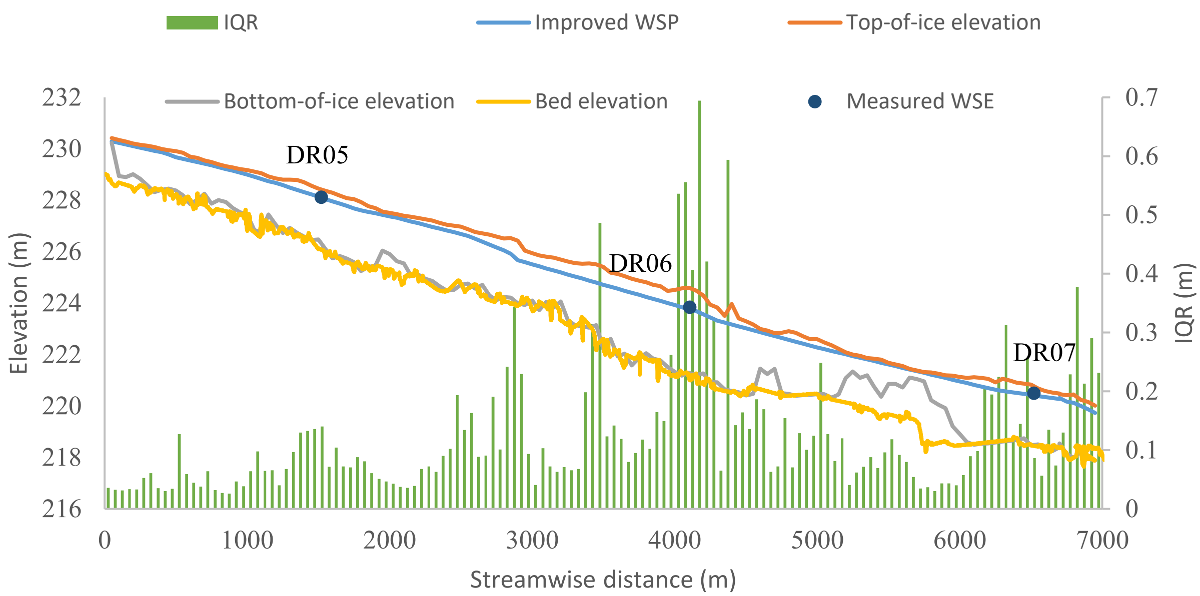

Figure 29. Corrected ice thickness profile for winter 2024/25, accompanied by ice surface IQR values representing roughness height at each cross-section.

4.3.3 Interpretation of Ice Thickness Profile 2023/24 and 2024/25

One of the most striking observations from the ice thickness profiles for both the winters of 2023/24 and 2024/25 was that the ice jam appears to have become grounded along nearly the entire study reach. While this may initially seem unrealistic, it can be explained by the geomorphological and climatic characteristics of the Dauphin River. Specifically, the river undergoes a transition from a relatively mild slope to a steeper gradient in the study area, which can promote the accumulation and thickening of ice jams. Moreover, the Dauphin River is naturally shallow and located in a region that experiences extremely cold winter temperatures. In November 2023 and November 2024, just before the freeze-up period, open-water discharge was approximately 65 and 75 cms, respectively, yielding water depths of about 1 m or less across the study reach.

As a result, even ice thicknesses such as 1.5 meters can lead to ice jam grounding in certain areas. Given these conditions, the widespread grounding observed is not unexpected. It is worth noting that had this study been conducted on a deeper river, the extent of grounding might have been significantly reduced. Figure 30 shows ice thickness profiles of winter 2023/24 and winter 2024/25 on the same plot. Maximum estimated ice thickness profiles are also shown on the plot.

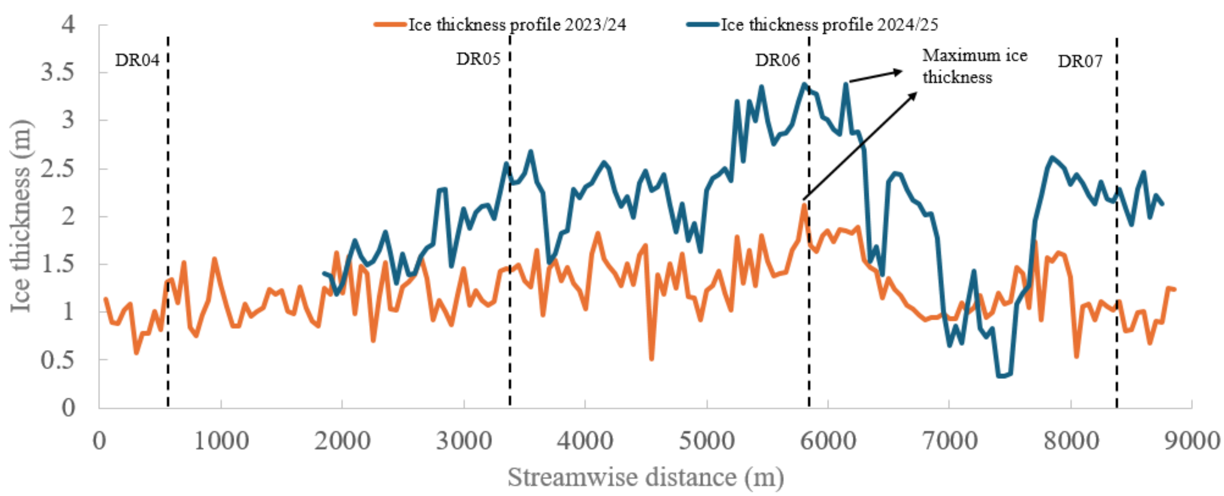

Figure 30. Estimated ice thickness profiles for winters 2023/24 and 2024/25 along the streamwise distance of the study area. Two black arrows indicate the peak ice thickness in each profile.

Another notable observation is the consistent spatial pattern of ice thickness formation between the winters of 2023/24 and 2024/25. A comparison of the corrected ice thickness profiles for both years reveals that the roughest section of the river, with the maximum ice thickness, is located near site DR06, which aligns with historical records of ice jam formation at this location. Additionally, in both years, certain sections upstream and downstream of DR05, as well as upstream of DR07, show areas where the ice jam did not become grounded. This recurring pattern supports the reliability of the applied methodology. Despite the fact that the ice thickness in winter 2024/25 was approximately one meter greater than in the previous year, the profiles remain consistent due to the river's geometric characteristics and the relatively similar discharge conditions. The agreement between these two independent datasets reinforces the validity of the grounding assessment and ice thickness estimation approach used in this study.

A comparison of the maximum estimated ice thickness between the two consecutive winters reveals a notable difference. In winter 2023/24, the maximum ice thickness of approximately 2.1 meters was observed just upstream of site DR06. In contrast, during winter 2024/25, the maximum ice thickness reached 3.37 meters, occurring right at site DR06, representing an increase of more than one meter compared to the previous year.

Two primary factors likely contributed to the formation of a thicker ice jam in the winter of 2024/25. The first is the difference in air temperature trends between the two winters, as illustrated in Figure 31, which covers the period from just before the onset of frazil ice generation to the completion of ice jam formation. Although the average air temperatures during this critical period were relatively similar, approximately -9.6 °C in 2024/25 and -6.5 °C in 2023/24, this modest difference alone does not fully explain the one-meter increase in ice jam thickness observed in 2024/25. However, a closer examination of the air temperature trends, as shown in Figure 28, reveals a notable contrast in the cooling patterns between the two years. In winter 2023/24, a sharp temperature drop occurred around November 23, likely triggering the onset of frazil ice production. This was immediately followed by a sudden warming event on November 25, with temperatures approaching 0°C and even rising above freezing in the following days. Such fluctuations could have led to partial melting of the initially formed frazil ice, reducing the overall volume available for consolidation. In contrast, during winter 2024/25, although the initial cooling was less abrupt, air temperatures remained consistently below freezing, fluctuating slightly around

-5 °C. This sustained sub-zero environment likely supported continuous frazil ice generation over an extended period. As a result, a larger volume of frazil ice may have accumulated and consolidated near site DR06, contributing to the formation of a significantly thicker ice jam in that year.

Furthermore, the cumulative degree-days of freezing (CDDF) for two consecutive winters, calculated from daily average air temperatures, were presented in Table 9. The CDDF for the 2023/24 winter was 76°C, while for 2024/25 it was 96°C, both calculated from November 21st up to December 2nd. This indicates that the colder conditions in 2024/25 favored greater frazil ice production, which in turn contributed to more pronounced consolidation events and the formation of thicker ice jams.

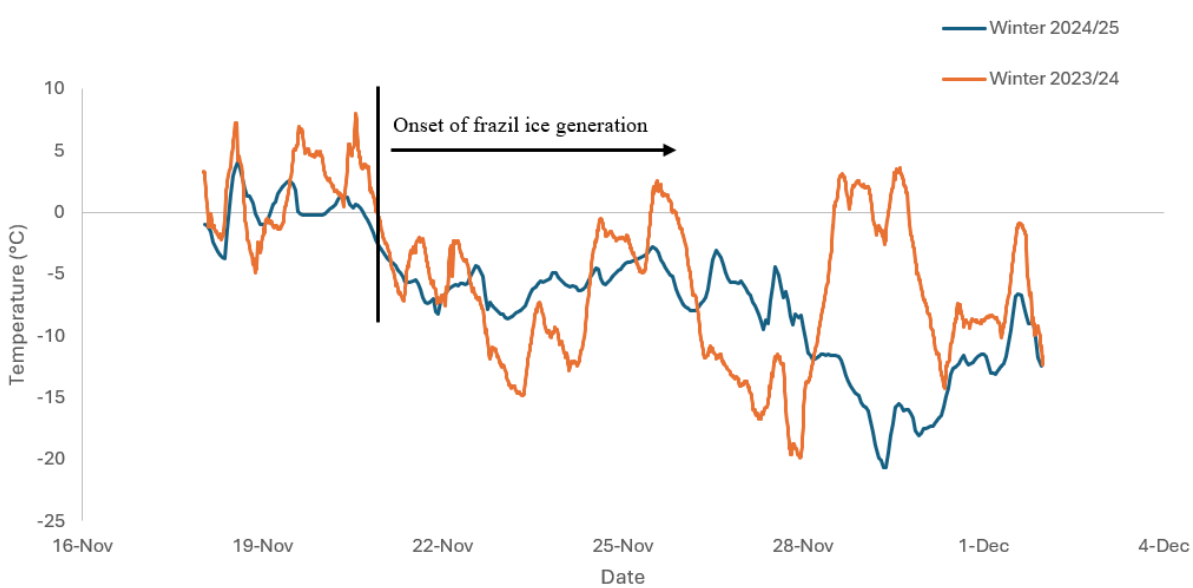

Figure 31. Comparison between air temperature before and during the freeze-up period for winter 2023/24 and winter 2024/25

Table 9. CDDF of winter 2023/24 and 2024/25 for the period of onset of frazil ice generation

	Average Daily Temperature (°C)	
Date	**2023-24**	**2024-25**
21-Nov	-4.5	-5.9
22-Nov	-7	-6.4
23-Nov	-11.3	-6.1
24-Nov	-6	-5.5
25-Nov	-1.1	-4.2
26-Nov	-10.2	-6
27-Nov	-15.6	-7.3
28-Nov	-3.8	-12.3
29-Nov	-0.2	-17.4
30-Nov	-9.7	-14.1
01-Dec	-6.8	-10.4
CDDF	**76.8**	**96.2**

Second, the open-water discharge immediately before freeze-up in 2024/25 was reported by the Survey of Canada to be approximately 5 to 10 m^3/s higher than in 2023/24. This elevated flow may have also contributed to increased frazil ice generation and more extensive consolidation events. It is worth noting that at the same site in winter 2018, Wazney et al. (2018) reported an ice thickness of 6 to 7 meters. However, during that year, the pre-freeze-up open-water discharge was approximately 210 m^3/s, three to four times higher than the discharge observed during the current study, highlighting the influence of hydrologic conditions on ice jam thickness.

Chapter 5 Surface Roughness Estimation Using LiDAR Data

5.1 Introduction to Surface Roughness

As discussed in Section 1.2.3Ice Roughness Estimation Using , the irregular features of surface ice can be used to estimate roughness height. Gadelmawla et al. (2002) introduced several parameters to characterize different aspects of surface roughness elevation. Their study emphasized that no single metric can fully describe all surface features. Therefore, in this research, three statistical parameters were focused on, each representing a different aspect of surface ice roughness. These statistical metrics were applied to the generated DEMs to provide a quantitative value of surface ice roughness.

5.1.1 Root Mean Square Roughness (RMS)

This parameter represents the standard deviation of elevation values within the selected area of the DEM. Root Mean Square (RMS) roughness increases with increased surface irregularity, meaning that rougher surfaces yield higher RMS values. It is a highly sensitive metric, as it accounts for every elevation variation in the dataset. As a result, rough sections exhibit larger RMS values, while smoother areas produce values closer to zero. Equation 7 shows the formula for calculation of RMS roughness:

Equation 7 $$R_q = \sqrt{\frac{1}{n}\sum_{i=1}^{n}(y_i - \bar{y})^2}$$

In this equation, n is the total number of data points in the selected sample, y_i is the elevation of each data point and $\bar{y}$ is the average elevation of data points along the selected sample.

5.1.2 Interquartile Range (IQR)

Interquartile Range (IQR) is a statistical metric that focuses on the central 50% of elevation variations. In other words, it excludes the extreme values in the lowest 25% and highest 25% of the dataset and is calculated by subtracting the 25th percentile from the 75th percentile. As reported by Ehrman et al. (2021), IQR is particularly effective for representing surface roughness height, especially when the dataset is non-normalized. When used alongside RMS, IQR can provide a more balanced understanding of surface variability. For instance, if a river cross-section contains an unusually high peak or deep valley, possibly due to ice chunk consolidation, RMS values may become significantly high due to these outliers. In contrast, IQR remains relatively unaffected by such extremes and may report a lower roughness value, indicating that most of the surface is smoother. This complementary behavior makes IQR a valuable addition for accurately interpreting surface ice roughness. Equation 8 represents the formula for calculating the IQR metric.

Equation 8 $$IQR = z_{Q_3} - z_{Q_1}$$

In equation 8, z_{Q_3} Shows the 75th percentile (i.e., third quartile) of the surface elevation values and z_{Q_1}represents the 25th percentile (i.e., first quartile) of the surface elevation.

5.1.3 Skewness (R_{sk})

The third statistical metric used to interpret surface roughness is skewness, which quantifies the asymmetry of a distribution relative to its mean. In the context of ice surface analysis, skewness indicates whether the elevation values in a selected area are more heavily influenced by peaks or valleys. Equation 9 presents the formula used to calculate skewness.

Equation 9 $$R_{sk} = \frac{1}{n}\sum_{i=1}^{n}\left(\frac{y_i-\bar{y}}{S}\right)^3$$

In Equation 9, y_i represents the elevation of each data point, $\bar{y}$ is the mean elevation of the selected area, S denotes the standard deviation, and n is the total number of data points. A positive skewness value indicates that peaks are predominant within the selected area, whereas a negative skewness suggests a dominance of valleys relative to the mean elevation. Skewness equal to zero indicates that the elevation distribution is approximately symmetric about its mean. In the next section, the captured datasets that will be used for roughness estimation will be shown.

5.2 Collected Dataset For Roughness Assessment Purposes

To quantify surface ice roughness during the winter of 2024/25, four separate survey missions were conducted at site DR06 to capture high-resolution datasets. Three of these missions utilized a LiDAR sensor, while one mission employed a photogrammetry payload to enable a comparative analysis between LiDAR and photogrammetry technologies.

As discussed in 3.4.1, the preliminary assessment concluded that using a single Ground Control Point (GCP) is sufficient to achieve high vertical accuracy in LiDAR surveys. However, this conclusion was based solely on LiDAR-based evaluations. In contrast, for the photogrammetry survey, the recommendation by Ehrman et al. (2021) that at least eight GCPs are required to achieve high-quality results was followed. Accordingly, eight GCPs were surveyed and established across the right bank, extending from near the road to the bushes and ultimately to the riverbank, in order to cover a wider area and capture different elevations for supporting the photogrammetry dataset processing. For the three LiDAR survey missions, the flight altitude was consistently set to 40 meters. However, the flight speeds were set to 2 m/s, 6 m/s, and 12 m/s to assess the impact of point cloud density on surface roughness estimation. Lower flight speeds result in denser point clouds, which are expected to provide more detailed surface representations, particularly relevant for analyzing the surface roughness of ice jams. In Figure 32, the generated DEMs from each separate mission are shown.

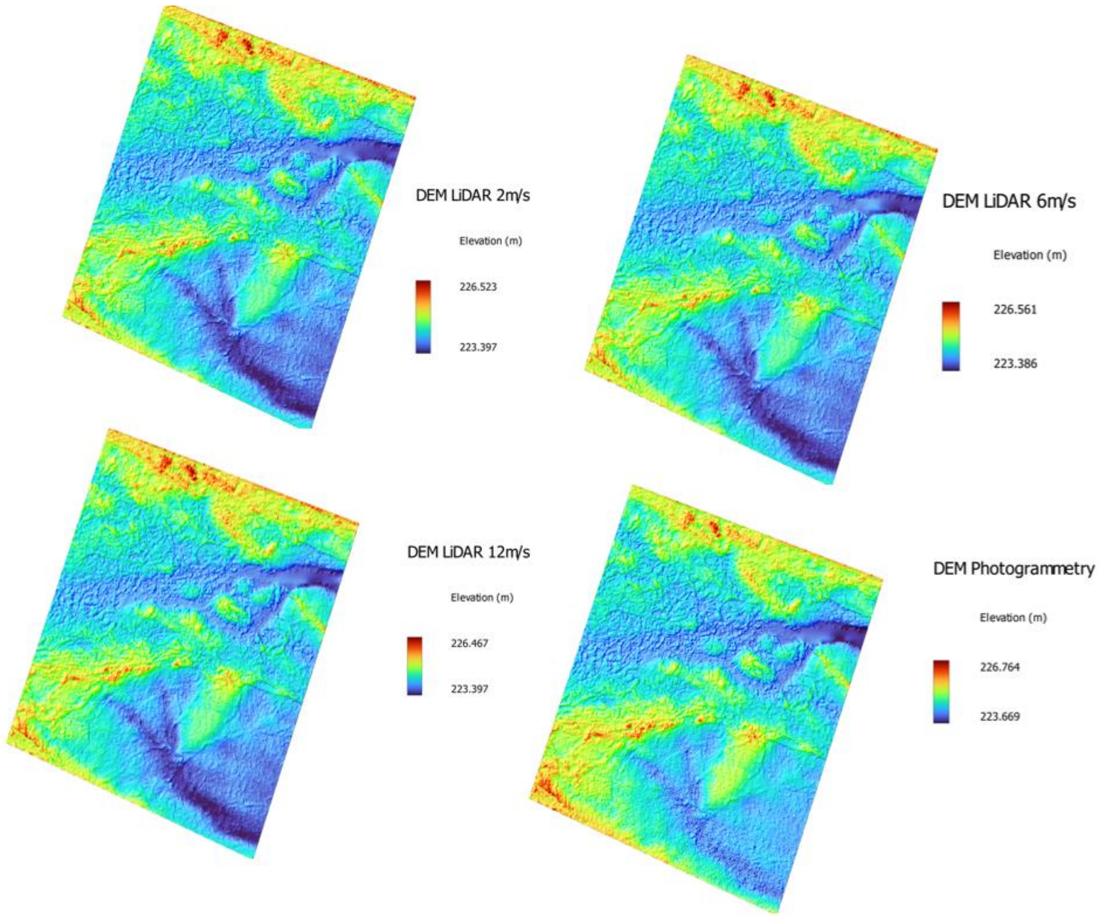

Figure 32. The generated DEMs from four separate missions will be used for surface roughness estimation.

The DEMs generated from the different survey missions resulted in varying spatial resolutions. The DEM from the LiDAR mission with a flight speed of 2 m/s, being the finest, has a resolution of 2.7 cm/pixel, followed by the LiDAR 6 m/s DEM at 4.3 cm/pixel, the photogrammetry DEM at 4.7 cm/pixel, and finally the LiDAR 12 m/s DEM at 5.0 cm/pixel.

From Figure 32, it can be observed that the three DEMs generated from LiDAR data are visually more consistent with one another compared to the DEM produced from the photogrammetry survey. Notably, the lowest elevation point in the photogrammetry dataset is 223.669 m, whereas the minimum elevation in the LiDAR-derived DEMs begins at 223.397 m, approximately 27 cm lower. This discrepancy prompted further investigation into the cause of the elevation difference. To explore this, a single transect was drawn from the left bank to the right bank of the river, and the elevation profiles from each DEM were extracted along this common transect. The resulting profiles are presented in Figure 33.

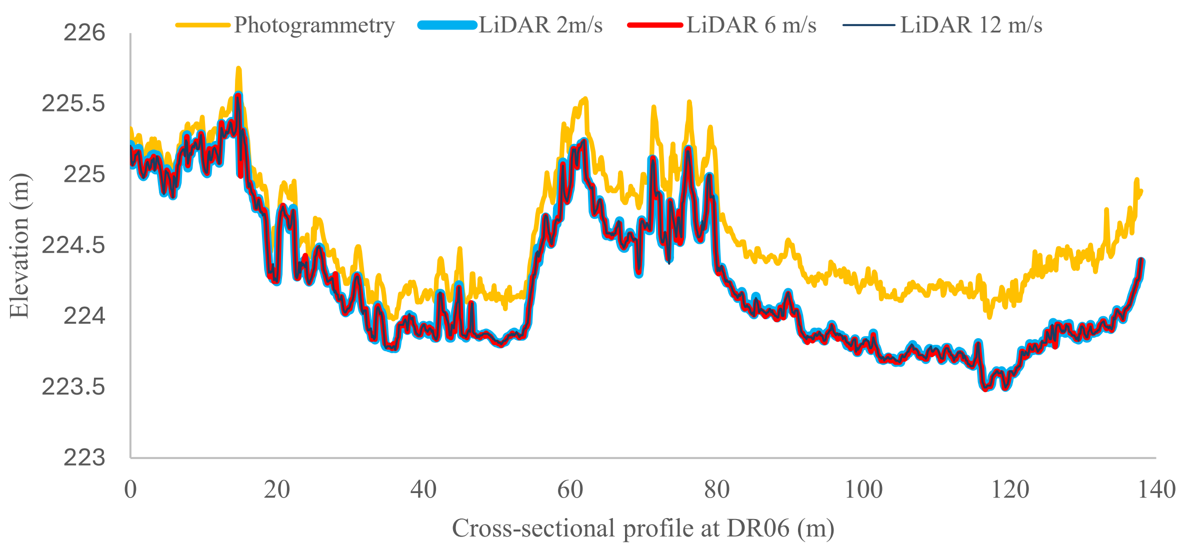

Figure 33. Comparison of the extracted elevation profiles between four different surveyed datasets.

The surface elevation profiles plotted along the transect show that all three LiDAR datasets, despite having different flight configurations, align closely and follow the same elevation pattern. In contrast, the photogrammetry dataset exhibits a noticeable and consistent upward shift across the transect. This discrepancy is most likely related to the distribution of GCPs. In contrast to the present survey, where GCPs were confined to one bank and none were placed on the river or the opposite bank, leading to a detectable vertical offset in the photogrammetric surface, Duguay et al. (2023) used the same P1 photogrammetric sensor but distributed GCPs across the entire reach, including on the frozen river and the opposite bank. With this balanced control geometry, they achieved accuracy comparable to their LiDAR survey, reporting an RMSE of approximately 0.06 m.

As observed in the profile, near the left bank, where the GCPs were concentrated, all four datasets align well. However, as the transect progresses toward the right bank, the photogrammetry data diverge upward from the LiDAR profiles. This trend is likely due to the nature of photogrammetry processing, in which elevations captured from GCPs are used to assign absolute heights to corresponding image features. From those control points, a triangulation-based interpolation process assigns elevations to the rest of the dataset. In our case, the lack of GCPs in the middle of the river and along the right bank caused an uneven distribution of control points. As a result, after the last GCP near the left bank, the software had to extrapolate elevation values across the remaining area. Even a small georeferencing error during this process can gradually accumulate, leading to significant elevation differences by the time the interpolation reaches the opposite bank. In this case, the accumulated error was approximately 50 cm near the opposite bank.

5.3 Evaluation of Surface Roughness from Collected Data

To utilize the captured datasets for surface roughness estimation, two sections were delineated within the surveyed area at site DR06. These sections were identified based on a visual assessment of the DEMs. One section near the left bank was selected to represent a rough ice jam, while another section near the right bank was chosen to represent a moderately rough ice jam. Since the survey was conducted at site DR06, no areas with smooth ice cover were identified within this section. For each of the two selected regions, one transect line and one area were defined in QGIS to extract elevation points from the DEMs. Each line is approximately 12 meters in length, and each area covers 200 m². Figure 34 illustrates a sample DEM along with the defined lines and areas over the rough and moderately rough sections.

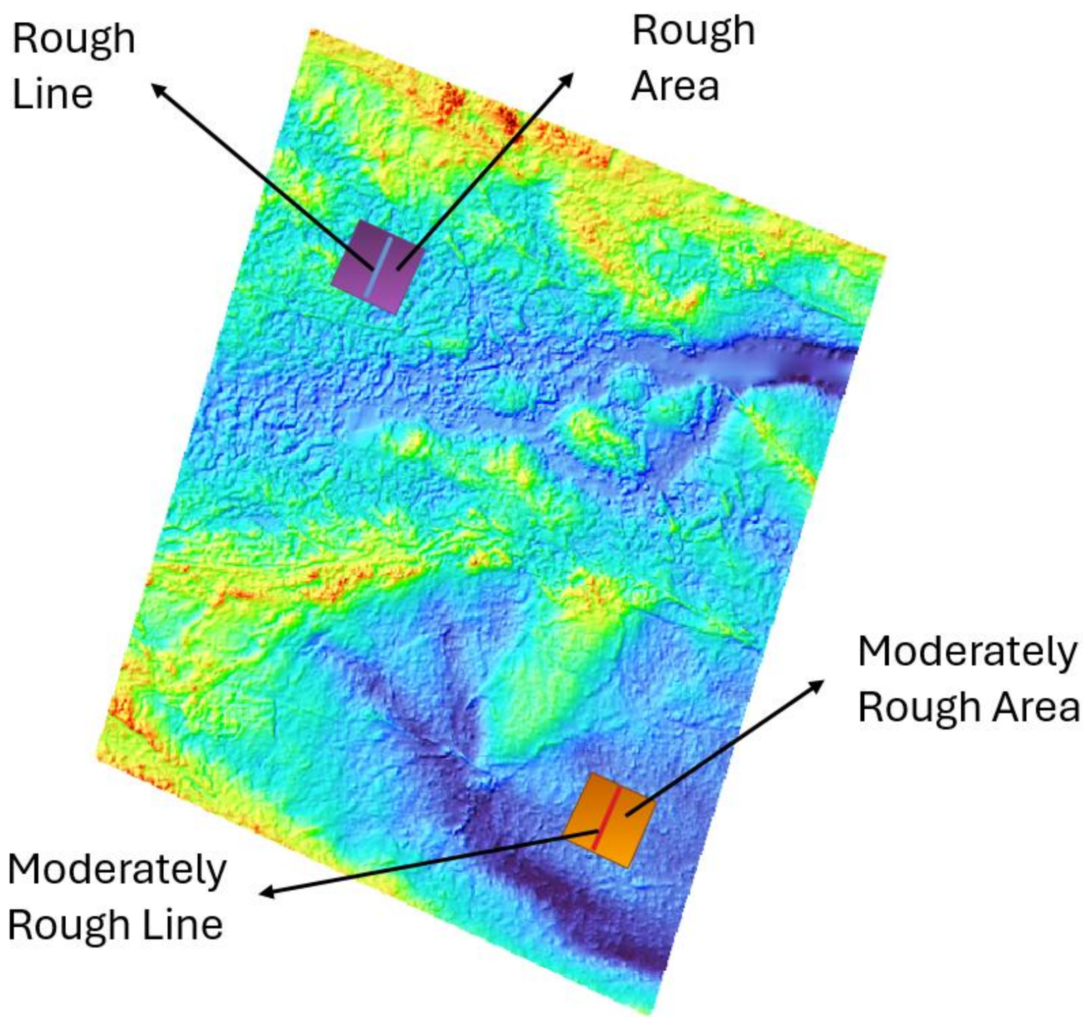

Figure 34. Illustration of the locations visually identified as rough and moderately rough, including the defined lines and areas.

The elevation data for each line and area were then extracted, and the selected statistical metrics (i.e., RMS, IQR, and skewness) were calculated for each sample. Table 10 summarizes the results of the statistical analysis for all samples.

Table 10. Summarizing the statistical analysis of selected samples for different survey missions.

Visual roughness assessment	Mission	Line			Area		
		RMS	IQR	R_{sk}	RMS	IQR	R_{sk}
Rough	LiDAR 12 m/s	0.146	0.113	0.908	0.177	0.228	0.696
	LiDAR 6 m/s	0.145	0.118	1.031	0.178	0.237	0.681
	LiDAR 2 m/s	0.146	0.123	0.927	0.180	0.239	0.692
	Photogrammetry	0.142	0.119	0.937	0.174	0.226	0.699
Moderately rough	LiDAR 12 m/s	0.057	0.083	0.677	0.053	0.064	0.141
	LiDAR 6 m/s	0.059	0.075	0.573	0.053	0.065	0.195
	LiDAR 2 m/s	0.059	0.089	0.538	0.054	0.075	0.187
	Photogrammetry	0.052	0.074	0.384	0.057	0.071	-0.309

The first point to emphasize is that the LiDAR 2 m/s dataset is expected to yield the most reliable results, as it offers the highest resolution among all missions. Therefore, comparing the results from this dataset with those from lower-resolution datasets allows us to assess the importance of data resolution in surface roughness estimation. It is important to note that RMS and IQR values represent the roughness height, whereas R_{sk} (skewness) is a statistical metric that reflects the dominance of peaks or valleys in the elevation data. As such, when evaluating the roughness estimation across different datasets, our focus is placed on comparing the RMS and IQR values within each group of samples (i.e., line and area) across different survey missions. This comparison provides insight into how data resolution influences the accuracy of roughness height estimation. It was observed that the differences in estimated roughness height between the various LiDAR datasets were generally less than 1 cm. Given the objective of this study, estimating surface roughness, such a difference is considered negligible. Therefore, considering both the minimal impact on roughness estimation accuracy and the significant reduction in survey time, conducting the LiDAR survey at a flight speed of 12 m/s appears to be the most efficient and practical approach under the given field conditions.

Based on Table 10, the calculated RMS and IQR values align well with our initial visual assessment of roughness in the two selected sections. Both metrics, RMS and IQR, are consistently higher in the rough section compared to the moderately rough section, for both the line and area samples. Notably, in the rough line sample, the RMS value exceeds the IQR, indicating the influence of sharp peaks on the RMS metric. This highlights the importance of including IQR in the analysis, as it is less sensitive to extreme values and better represents the central variability of the dataset by focusing on the middle 50%.

In contrast, for the remaining three groups (i.e., rough area, moderately rough line, and moderately rough area), the IQR values are greater than the RMS values. This suggests that in these cases, surface roughness is more broadly distributed across the dataset, rather than being driven by isolated peaks. The complementary nature of RMS and IQR thus provides a more comprehensive understanding of surface roughness characteristics.

R_{sk} shows a positive value across all datasets, except for the photogrammetry dataset in the moderately rough area sample. A positive R_{sk} value indicates that peaks are more dominant, while the negative R_{sk} value observed in the photogrammetry dataset suggests a predominance of valleys. This discrepancy may be attributed to the known systematic vertical error in the photogrammetry data, potentially distorting the elevation distribution and leading to an inaccurate skewness result.

Finally, the RMS and IQR values obtained from the area-based analysis show noticeable differences compared to those from the line-based analysis, as presented in Table 10. These differences suggest that roughness estimates derived from a single transect may be biased due to the presence of isolated peaks or depressions intersecting the line. In contrast, area-based analysis incorporates a larger number of elevation points, reducing the influence of local anomalies and providing a more representative and reliable assessment of surface roughness across the study area. Consequently, in Section 5.4, the roughness analysis is repeated using the IQR metric, which is less sensitive to outliers and extreme values, rather than relying on a single perpendicular transect. An area-based approach is adopted for each cross-section to estimate roughness for the winter 2024/25 ice thickness profile plot.

5.4 Estimation of Roughness Height Along the River Using Buffers

In this section, the captured DEM covering the entire 7 km stretch of the Dauphin River was used to estimate surface roughness at 50 m intervals along the river using the IQR metric in an area-based approach. IQR was selected for this analysis because it is less sensitive to outliers and, as reported by Ehrman et al. (2021), performs more reliably when applied to non-normalized datasets. Based on the conclusions from the previous section, area-based roughness estimation provides more accurate and representative insight into surface roughness characteristics. Following the methodology outlined in Section 4.1.1, each previously defined perpendicular cross-section line was expanded into a buffer zone by extending 10 m on either side, resulting in buffer polygons 20 m long in the streamwise direction and the same width as the original cross-section lines. Figure 35 illustrates the defined buffer zones over the winter 2024/25 DEM.

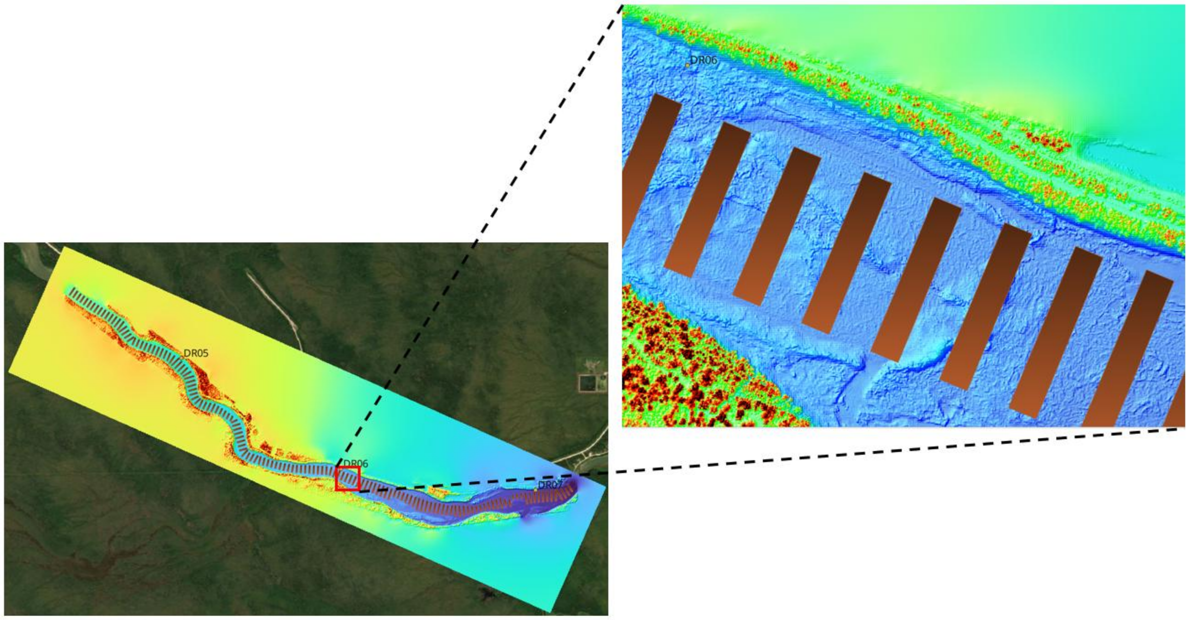

Figure 35. Illustration of buffer layers along 7 km of the river with an interval of 50 m over the DEM winter 2024/25.

Next, the buffer layers were used to extract elevation data from the underlying DEM. Figure 36 illustrates the complete process, from defining the buffer lines to extracting elevation values from the DEM.

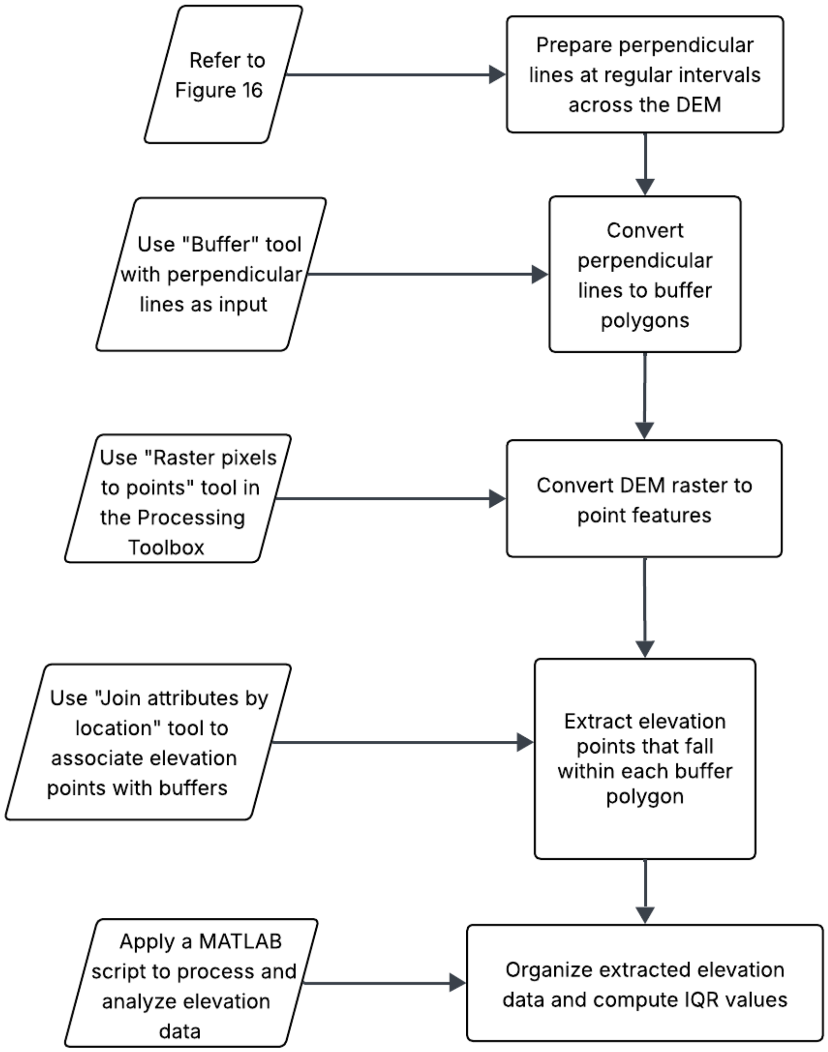

Figure 36. Flowchart outlining the processing steps for extracting elevation data from defined buffer zones using QGIS software.

All of the steps described above were followed, and the resulting IQR values for each buffer layer were plotted along with the ice thickness profile derived in Section 4.3.2 in Figure 37.

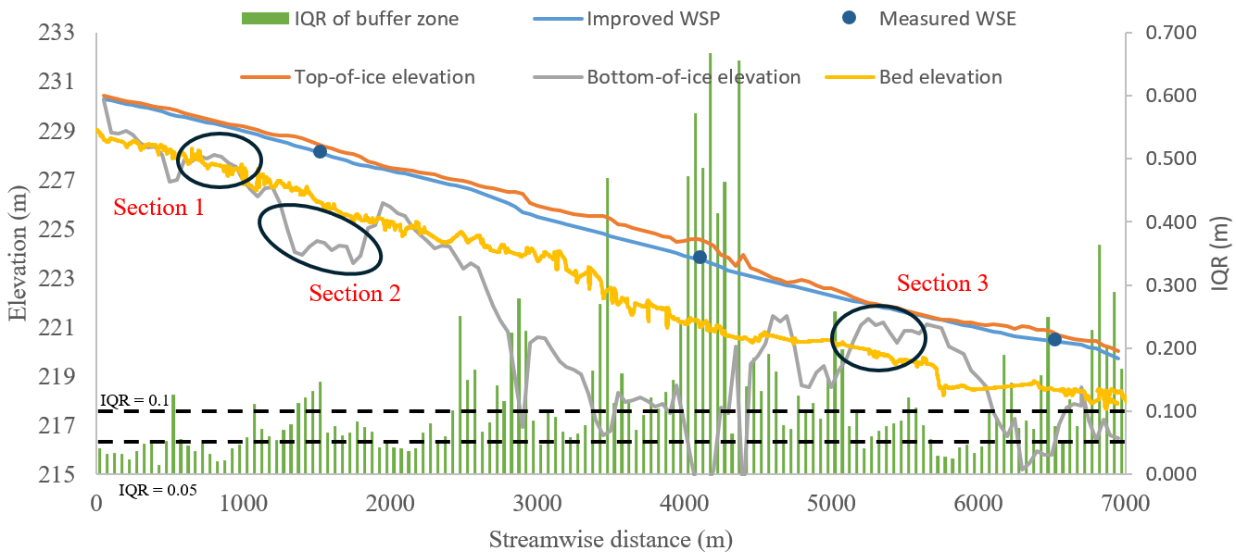

Figure 37. Ice Thickness Profile for Winter 2024/25 Alongside Interquartile Range (IQR) Estimates from Buffer Zone Analysis.

In Figure 37Figure 37, the extracted IQR values from the buffer zone analysis are presented using green column bars. The calculated IQR values range from approximately 0.03 m to 0.7 m, with lower values indicating smoother ice surfaces and higher values representing significantly rougher ice conditions. Based on the relationship between IQR values and observed grounding of the ice jam, three categories of surface roughness were defined.

- For IQR values below 0.05 m, the ice surface was classified as relatively smooth, with no observed grounding, such as in Section 1.
- For IQR values exceeding 0.10 m, the surface was classified as rough, and grounding occurred consistently in these cross-sections.
- For IQR values between 0.05 m and 0.10 m, the surface was considered moderately rough. Grounding in this range appears to be influenced by local bathymetric conditions. For example, in Section 3, although IQR values fell within this intermediate range, the ice jam did not become grounded.

In the previous chapter, the corresponding IQR values for each cross-section were calculated using a line-based approach. In this chapter, the IQR values were obtained using a buffer-based approach, and the results of both methods are compared in Figure 38 using a proportionality plot. Most data points show a strong correlation between the two methods, with an R^2 value of 0.92. However, a few points exhibit noticeable differences. Two points plotted above the 1:1 line indicate that the buffer-based approach produced higher IQR values than the line-based method. Further investigation revealed that these points correspond to site DR06, which represents the roughest section in the dataset. This suggests that the line-based approach underestimated roughness in these sections, whereas the buffer-based method, by incorporating elevation variations over an area rather than a single transect, captured greater variability and produced higher IQR values. Conversely, two points were located below the 1:1 line, indicating that the line-based method overestimated roughness compared to the buffer-based approach. These points correspond to sections near site DR07, where ice thickness was relatively thin compared to other sites, consistent with lower roughness. Overall, although both methods demonstrated strong correlation, the buffer-based approach was found to be more accurate, as it accounts for elevation variability across an area rather than along a single line.

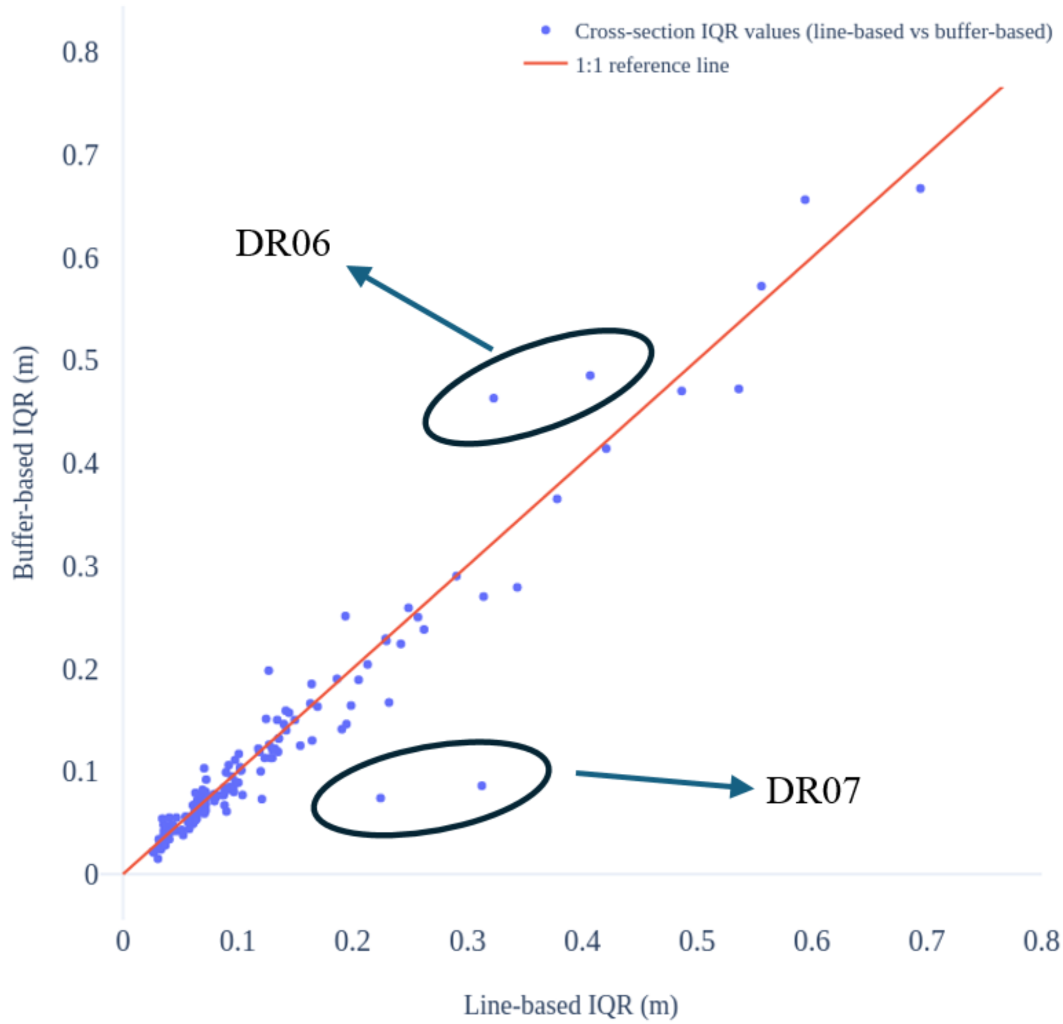

Figure 38. Proportionality plot of line-based vs buffer-based IQR values with noticeable deviations near DR06 (underestimation) and DR07 (overestimation)

This classification highlights the usefulness of IQR as a reliable proxy for quantifying surface ice roughness and its potential application in identifying zones susceptible to ice jam grounding. It is important to note, however, that the IQR thresholds defined in this study are specific to the hydraulic and geomorphological conditions of the Dauphin River. As such, these threshold values should not be directly transferred to other study sites without careful consideration. Nonetheless, the overall methodology presented here offers a transferable framework that can be applied to other river systems to characterize surface roughness and assess ice jam behavior.

Chapter 6 Conclusions

This research focused on the observation, analysis, and interpretation of river ice processes on the Dauphin River, with an emphasis on top-of-ice elevation, ice thickness, surface roughness, and their hydraulic implications. River ice plays a critical role in controlling water levels during winter (i.e., freeze-up period) and breakup periods, and ice jams in particular can produce extreme backwater effects that threaten nearby communities. Understanding these processes requires comprehensive datasets that capture both hydraulic and ice conditions. However, traditional monitoring techniques, which often rely on point surveys along the riverbanks, have historically been limited in coverage, resolution, and safety, especially during unstable jam conditions. This work sought to overcome these challenges through the combined use of conventional field instrumentation and advanced airborne remote sensing.

A variety of field instruments were deployed along the Dauphin River to track winter ice processes. Level loggers, temperature loggers, and trail cameras provided continuous records of water level fluctuations, freeze-up timing, and ice cover conditions throughout the winter. These observations made it possible to identify the onset of frazil production and to pinpoint the timing of freeze-up jams during both the 2023/24 and 2024/25 winters. Such information is invaluable for linking hydrometric changes to ice events and establishing ground truth for further analysis.

Building on this foundation, airborne LiDAR surveys conducted with a Matrice-350 RPA equipped with a Zenmuse L2 sensor provided a major advance in data acquisition. Surveys in

February 2024 and December 2024 mapped nearly 9 and 7 km of frozen river surface at high spatial resolution, respectively. The resulting point clouds and DEMs offered unprecedented accuracy, with a root mean square error of less than six centimeters after ground control adjustment. These datasets enabled the construction of continuous top-of-ice elevation profiles along long river reaches, something previously unattainable through traditional surveying. Unlike conventional methods limited to bank-accessible points, airborne data captured conditions across the full channel width, including the central and roughest zones of the ice cover, where direct access was impossible.

The availability of both top-of-ice and water surface elevation data allowed for innovative methods of ice thickness estimation. Where ice was grounded, thickness could be derived by subtracting bathymetric elevations from the measured ice surface. In floating jam reaches, thickness was estimated using the freeboard concept, accounting for the buoyant balance between ice and water. This approach provided thickness estimates even where direct measurement was impractical, particularly in rough or consolidated sections where ice exceeded two meters in thickness. Such estimates are critical for understanding the structural characteristics of jams and their hydraulic influence.

Surface roughness was quantified using statistical metrics applied to the high-resolution DEMs. Root Mean Square (RMS) and Interquartile Range (IQR) values were used to evaluate roughness heights, with IQR emerging as the more robust measure due to its insensitivity to extreme anomalies. Buffer-based analyses along 50 m intervals revealed strong correlations between elevated IQR values and jam grounding locations, enabling thresholds to be defined for assessing grounding potential specifically for this study site. This provided a spatially continuous method for identifying likely jam consolidation zones, offering new insight into where and how jams exert the greatest hydraulic impacts.

Together, these methods produced one of the most comprehensive river ice datasets to date, integrating continuous top-of-ice profiles, ice thickness estimates, roughness metrics, and supporting hydrometric records. The outcomes demonstrate how advanced remote sensing can transform ice monitoring from discrete, hazardous surveys into high-resolution, system-wide analyses. Importantly, these datasets are not only valuable for understanding the dynamics of the Dauphin River but also provide critical input for numerical modeling. Ice jam models rely on parameters such as ice thickness, roughness, and water surface elevation for calibration and validation. By providing detailed site-specific data, this research reduces the dependence on uncertain parameter assumptions, thereby enhancing the predictive capacity of ice jam simulations.

In conclusion, this research demonstrates the effectiveness of combining field-based monitoring with advanced airborne LiDAR to investigate river ice processes. The resulting datasets provided new opportunities for analyzing freeze-up and ice jam events with unprecedented detail, while offering direct benefits for numerical model calibration. Beyond the Dauphin River, the methods developed here are broadly applicable to other cold-region rivers where ice jams pose hazards to communities and infrastructure. By bridging observational gaps and enhancing the tools available for simulation and prediction, this work contributes to more robust, data-driven approaches to river ice engineering and flood management.

6.1 Future work

Analysis of the level logger data from the winters of 2023/24 and 2024/25 revealed a sudden rise in water levels during the breakup period, with a more pronounced increase observed in 2024/25.

This pattern suggests the potential occurrence of a breakup ice jam. While the present study focused solely on the freeze-up period and associated ice jam formation, future research should extend to include detailed investigations of breakup ice jams at this study site to provide a more comprehensive understanding of ice-related hydraulic dynamics.

In the 2023/24 season, only four level loggers were deployed within the LiDAR-surveyed area, and in 2024/25, due to the exclusion of site DR04 from the LiDAR survey, only three level loggers were available for validation. This limited the number of reliable validation points for comparing extracted water surface elevations from LiDAR data with actual field measurements. Future studies should consider deploying additional level loggers across the surveyed reach to enhance the spatial coverage and improve the accuracy of water surface elevation validation.

Although this study aimed to validate all captured data using aerial surveys, no direct measurements of ice thickness were available for the Dauphin River. As a result, there were no independent datasets to validate the ice thickness estimates derived from the proposed method. Future research should incorporate direct field measurements of ice thickness at selected locations or apply alternative remote sensing techniques, such as Ground Penetrating Radar (GPR) or other radar-based sensors, to generate independent estimates. These additional data sources would provide valuable validation points for assessing the accuracy of the estimated ice thickness profiles.

The method developed in this study for estimating ice jam thickness and surface roughness should be applied to other river systems, particularly deeper rivers with fewer grounded ice jam areas, to generate more reliable datasets for numerical modeling. Additionally, future work should focus on identifying comparable IQR-based thresholds across multiple study sites. By analyzing patterns in surface roughness, subsurface roughness, and ice jam grounding across various rivers, a deeper understanding of the relationship between surface characteristics and ice jam mechanics can be achieved. This could contribute significantly to the development and calibration of ice jam models.

The parameters captured in this study provide a comprehensive dataset for monitoring freeze-up ice jams. Developing a numerical model for the same study site and incorporating the collected data to simulate ice jam formation would offer an excellent opportunity to validate and refine ice jam modeling approaches. Comparing model outputs with the estimated ice thickness and roughness values from this study could significantly enhance the accuracy and reliability of numerical models in river ice research.

Chapter 7 References

American Society for Photogrammetry and Remote Sensing. (2023). ASPRS positional accuracy standards for digital geospatial data (Edition 2, Version 1.0). https://www.asprs.org/standards/

Ban, Y., (2016). Multitemporal remote sensing: current status, trends and challenges. In: Remote Sensing and Digital Image Processing, pp. 1–18. https://doi.org/10.1007/ 978-3-319-47037-5_1

Barrette, P. D., Khan, A. A., & Lindenschmidt, K. E. (2024). A glance at 25 process-based hydraulic models for river ice. In Proceedings of the 27th International Symposium on Ice. International Association for Hydro-Environment Engineering and Research (IAHR), Gdańsk, Poland.

Beltaos, S. (2001). Hydraulic roughness of breakup ice jams. Journal of Hydraulic Engineering, 127(8),650-656.

Beltaos, S. (2008). Progress in the study and management of river ice jams. Cold regions science and technology, 51(1), 2-19.

Beltaos, S., & Burrell, B. C. (2010). Ice-jam model testing: Matapedia River case studies, 1994 and 1995. Cold Regions Science and Technology, 60(1), 29-39.

Beltaos, S., & Tang, P. (2013, July). Applying HEC-RAS to simulate river ice jams: snags and practical hints. In Proc. 17th Workshop on River Ice, held at Edmonton (pp. 21-24).

Bhardwaj, A., Sam, L., Bhardwaj, A., & Martín-Torres, F. J. (2016). LiDAR remote sensing of the cryosphere: Present applications and future prospects. Remote Sensing of Environment, 177, 125-143.

Blackburn, J., & She, Y. (2023). The simulation of ice jam profiles in multi-channel systems using a one-dimensional network model. Cold Regions Science and Technology, 208, 103796.

Carson, R., Beltaos, S., Groeneveld, J., Healy, D., She, Y., Malenchak, J., ... & Shen, H. T. (2011). Comparative testing of numerical models of river ice jams. Canadian Journal of Civil Engineering, 38(6), 669-678.

Clark, S. P., & Wall, A. (2016). Freeze-up monitoring on the Dauphin River, Manitoba, Canada. In Proceedings of the 23rd International Symposium on Ice. International Association of Hydro-Environment Engineering and Research, Ann Arbor, Michigan (p. 10).

Dammann, D. O., Eicken, H., Mahoney, A. R., Saiet, E., & Meyer, F. J. (2017). Traversing sea ice—linking surface roughness and ice trafficability through SAR polarimetry and interferometry. IEEE Journal of Selected Topics in Applied Earth Observations and Remote Sensing, 11(2), 416-433.

DJI. (2023). Zenmuse L2 user manual (Version 1.0). https://www.dji.com

Ehrman, J., Clark, S., & Wall, A. (2021). Ice roughness estimation via remotely piloted aircraft and photogrammetry. The Cryosphere, 15(8), 4031-4046.

Gadelmawla, E. S., Koura, M. M., Maksoud, T. M. A., Elewa, I. M., & Soliman, H. H. (2002). Roughness parameters. Journal of Materials Processing Technology, 123(1), 133–145. https://doi.org/10.1016/S0924-0136(02)00060-2

Graf, R., & Tomczyk, A. M. (2018). The impact of cumulative negative air temperature degree-days on the appearance of ice cover on a river in relation to atmospheric circulation. Atmosphere, 9(6), 204.

Hicks, F. E. (2016). An introduction to river ice engineering for civil engineers and geoscientists. CreateSpace Independent Publishing Platform.

Jin, H., Yao, X., Wei, Q., Zhou, S., Zhang, Y., Chen, J., & Yu, Z. (2024). Ice Thickness Assessment of Non-Freshwater Lakes in the Qinghai–Tibetan Plateau Based on Unmanned Aerial Vehicle-Borne Ice-Penetrating Radar: A Case Study of Qinghai Lake and Gahai Lake. Remote Sensing, 16(6), 959.

Lindenschmidt, K. E. (2020). River ice processes and ice flood forecasting. Springer International Publishing.

Lindenschmidt, K. E., Sydor, M., & Carson, R. W. (2012). Modelling ice cover formation of a lake–river system with exceptionally high flows (Lake St. Martin and Dauphin River, Manitoba). Cold Regions Science and Technology, 82, 36-48.

Lindenschmidt, K. E., Sydor, M., van der Sanden, J., Blais, E., & Carson, R. W. (2013, July). Monitoring and modeling ice cover formation on highly flooded and hydraulically altered lake-river systems. In 17th CRIPE Workshop on the Hydraulics of Ice Covered Rivers, Edmonton, AB, Canada (pp. 21-24).

Lindenschmidt, K. E., Syrenne, G., & Harrison, R. (2010). Measuring ice thicknesses along the Red River in Canada using RADARSAT-2 satellite imagery. Journal of Water Resource and Protection, 2(11), 923-933.

Lindenschmidt, K.-E. (2017). RIVICE—A non-proprietary, open-source, one-dimensional river-ice model. Water, 9(5), 314. https://doi.org/10.3390/w9050314.

Lindenschmidt, K.-E., Basnet, G., Nafziger, J., Lees, K., Beltaos, S., & Blackburn, J. et al. (2025). Simulation comparison of river-ice hydraulic models. 23rd Workshop on the Hydraulics of Ice-Covered Rivers.

Liu, B., Ji, H., Zhai, Y., & Luo, H. (2023). Estimation of river ice thickness in the Shisifenzi reach of the Yellow River with remote sensing and air temperature data. IEEE Journal of Selected Topics in Applied Earth Observations and Remote Sensing, 16, 5645-5659.

Liu, L., Li, H., & Shen, H. T. (2006, August). A two-dimensional comprehensive river ice model. In Proceedings of the 18th IAHR symposium on river ice, Sapporo, Japan (Vol. 28).

Nezhikhovskiy, R. A. (1964). Coefficients of roughness of bottom surface of slush-ice cover. Soviet hydrology, 2, 127-150.

Nolin, A. W., & Mar, E. (2018). Arctic sea ice surface roughness estimated from multi-angular reflectance satellite imagery. Remote Sensing, 11(1), 50.

Pelletier, P. M. (1990). A Review of Techniques used by Canada and other Northern Countries for Measurement and Computation of Streamflow under Ice Conditions: Paper presented at the 8th Northern Res. Basins Symposium/Workshop (Abisko, Sweden-March 1990). Hydrology Research, 21(4-5), 317-340.

Shen, H. T., Su, J., & Liu, L. (2000). SPH simulation of river ice dynamics. Journal of Computational Physics, 165(2), 752-770.

Strickler, A.: Contributions to the Question of a Velocity Formula and Roughness Data for Streams, Channels and Closed Pipelines, Tech. Rep. 16, Swiss Department of the Interior, Bureau of Water Affairs, 1923.

Wazney, L., Clark, S. P., & Malenchak, J. (2019). Effects of freeze-up consolidation event surges on river hydraulics and ice dynamics on the Lower Dauphin River. Cold Regions Science and Technology, 158, 264-274.

Wazney, L., Clark, S. P., & Malenchak, J. (2019). Laboratory investigation of the consolidation resistance of a rubble river ice cover with a thermally grown solid crust. Cold Regions Science and Technology, 157, 86-96.

Wazney, L., Clark, S. P., & Wall, A. (2017, July). Freeze-up jam observations on the Dauphin River. In Proceedings of the 19th Workshop on the Hydraulics of Ice Covered Rivers. Committee on River Ice Processes and the Environment, Whitehorse, Yukon, Canada (p. 21).

Wazney, L., Clark, S. P., & Wall, A. J. (2018). Field monitoring of secondary consolidation events and ice cover progression during freeze-up on the Lower Dauphin River, Manitoba. Cold Regions Science and Technology, 148, 159-171.

Yao, H., Qin, R., & Chen, X. (2019). Unmanned aerial vehicle for remote sensing applications—A review. Remote Sensing, 11(12), 1443.

Zakharov, I., Puestow, T., Khan, A. A., Briggs, R., & Barrette, P. (2024). Review of River Ice Observation and Data Analysis Technologies. Hydrology, 11(8), 126.